The 5–6 December 1991 FIRE IFO II Jet Stream Cirrus Case Study: Possible Influences of Volcanic Aerosols

KENNETH SASSEN,* DAVID O'C. STARR,† GERALD G. MACE,# MICHAEL R. POELLOT,@ S. H. MELFI,† WYNN L. EBERHARD,& JAMES D. SPINHIRNE,† E. W. ELORANTA,** DONALD E. HAGEN,†† AND JOHN HALLETT##

*Meteorology Department, University of Utah, Salt Lake City, Utah
†NASA Goddard Space Flight Center, Greenbelt, Maryland
#Meteorology Department, The Pennsylvania State University, University Park, Pennsylvania
@Atmospheric Sciences Department, University of North Dakota, Grand Forks, North Dakota
&NOAA Environmental Technology Laboratory, Boulder, Colorado
**Meteorology Department, University of Wisconsin, Madison, Wisconsin
††Physics Department, University of Missouri, Rolla, Missouri
##Desert Research Institute, Reno, Nevada

(Manuscript received 14 January 1994, in final form 25 May 1994)

ABSTRACT

In presenting an overview of the cirrus clouds comprehensively studied by ground-based and airborne sensors from Coffeyville, Kansas, during the 5–6 December 1992 Project FIRE IFO II case study period, evidence is provided that volcanic aerosols from the June 1991 Pinatubo eruptions may have significantly influenced the formation and maintenance of the cirrus. Following the local appearance of a spur of stratospheric volcanic debris from the subtropics, a series of jet streaks subsequently conditioned the troposphere through tropopause foldings with sulfur-based particles that became effective cloud-forming nuclei in cirrus clouds. Aerosol and ozone measurements suggest a complicated history of stratospheric–tropospheric exchanges embedded within the upper-level flow, and cirrus cloud formation was noted to occur locally at the boundaries of stratospheric aerosol-enriched layers that became humidified through diffusion, precipitation, or advective processes. Apparent cirrus cloud alterations include abnormally high ice crystal concentrations (up to ~600 L^{-1}), complex radial ice crystal types, and relatively large haze particles in cirrus uncinus cell heads at temperatures between −40° and −50°C. Implications for volcanic–cirrus cloud climate effects and usual (nonvolcanic aerosol) jet stream cirrus cloud formation are discussed.

1. Introduction

A major focus of climate research is, of necessity, the climatological characterization of the current state of the cloudy atmosphere. Such knowledge is requisite in order to assess the validity of cloud predictions from global general circulation models and also, in general, to better understand the effects of cloud radiative forcing and feedbacks on climate, present or future. The essentially continuous observations provided by earth-orbiting satellites obviously have significant advantages in this endeavor, and the International Satellite Cloud Climatology Project (ISCCP) represents a long-term program to employ satellite data to gain knowledge of the amounts and types of cloud cover (Schiffer and Rossow 1983). Unfortunately, whereas cirrus clouds are certainly an important component of this dataset, it is recognized that they represent a particularly difficult cloud category to detect and categorize. This is because cirrus clouds are composed of relatively dilute assemblies (i.e., in comparison to water clouds) of complexly shaped ice crystals that are by definition optically thin in the visible and greybody emitters in the infrared spectral regions (Platt et al. 1987).

To help overcome the deficiencies in our basic knowledge of cirrus clouds and improve our ability to characterize them from satellite radiance measurements, the First ISCCP Region Experiment (FIRE) has been established (Cox et al. 1987). The initial Intensive Fields Observation (IFO) program was conducted over central and southern Wisconsin in October–November 1986 and utilized three research aircraft and an array of four ground-based lidar systems. (For a description of prior case study findings based on aircraft, lidar, and satellite studies, see the November 1990 special issue of *Monthly Weather Review*.) The IFO II program recently took place during November–December 1991 and brought together an even greater collection of state of the art in situ and

Corresponding author address: Dr. Kenneth Sassen, Department of Meteorology, University of Utah, 819 William C. Browning Building, Salt Lake City, UT 84112.

TABLE 1. Specifications of the FIRE IFO II remote sensing systems, as configured during the experiment at Coffeyville, Kansas. Entries v, h, and c refer to vertical, horizontal, and circular polarization properties.

	University of Utah PDL	NOAA WPLDL	NASA RAMAN	NASA ER-2 CALS	PSU W-band radar
Transmitter					
Type	NdYAG	CO_2	XeF	NdYAG	Clystron
Wavelength (μm)	0.532	10.6	0.351	0.532	3.2×10^4
Peak energy (J)	0.5	1.0	0.045	0.04	200
Pulse length (ns)	7	300	20	5.0	500
Maximum PRF (Hz)	10	10	400	5.0	20×10^3
Beamwidth (mrad)	0.45	0.05	~0.5	1.0	4.36
Polarization	v	c	—	v	v
Receiver					
Diameter (m)	0.35	0.25	0.76	0.15	0.91
Beamwidth (mrad)	0.3–4.0	0.05	2	1.4	4.36
Polarization	$v + h$	—	—	$v + h$	v
Detectors	2	1	8	2	1
Scanning ($^\circ$ s^{-1})	(Manual)	30	(Fixed)	(Fixed)	(Fixed)
Data handling					
Range resolution (m)[a]	6.0	75	75	7.5	75
Number of channels	2	1	8	2	1
Samples per channel	2048	20	600	3072	506
Pulses averaged	1–10	1–10	23200	1	1000–20000
Data quantities[b]	P, δ	P, β_π, V	P, β_π, σ_π, w	P, δ	Z_e

[a] Effective minimum resolution.

[b] Relative returned power P; backscatter cross section β_π; linear depolarization ratio δ; radial Doppler velocity V; extinction cross section σ_π; water vapor mixing ratio w; equivalent radar reflectivity factor Z_e.

TABLE 2. Special aerosol, ozone, and microphysical apparatus deployed on the indicated Project FIRE aircraft, providing data used in this study.

University of North Dakota Citation	
Ozone	
Manufacturer/model	Scientrex/LOZ3
Type	Chemiluminescent
Range	0.2 to 400 ppb
Resolution	0.1 ppb
Accuracy	±10%
Response	1 s
Condensation Nuclei	
Manufacturer/model	TSI/3760
Type	Alcohol condensing
Range	$0–10^4$ cm^{-3}
Resolution	1 cm^{-3}
Accuracy	±6%
Response	2 s
Replicator	
Manufacturer/model	Desert Research Institute
Type	Continuous Formvar
Range	~10–1000 μm
NCAR Saberliner	
Tandem electric aerosol classifiers	
Manufacturer	UMR
Range	0.01–0.5 μm
Resolution	±5%
Accuracy	±5%
Response	2 min

remote sensing instruments for studying cirrus clouds over Coffeyville, Kansas.

It is the early results from an interesting IFO II cirrus cloud case study involving a significant departure from the conditions encountered during the IFO I that are reported here. The global atmospheric effects created by the explosive June 1991 eruptions of the Philippine volcano Pinatubo presented an opportunity to investigate the possible effects on cirrus cloud formation of stratospherically derived volcanic aerosols (Sassen and Horel 1990; Mohnen 1990; Sassen 1992). Beginning on the evening and dawn of 4 December 1991, spectacular twilight effects indicative of a sudden increase in volcanic aerosols were noted by IFO observers. These kinds of events accompanied the latitudinal redistribution of the Pinatubo debris as spurs of stratospheric aerosols were lifted from the tropical zonal belt, aided by jet stream circulations in both hemispheres (GVN Bulletins 1991–1993). The series of jet streak cirrus cloud systems that were subsequently studied over southeastern Kansas yielded indications of unusual cloud properties, suggesting a link between the volcanic aerosols, tropopause-folding effects, and cirrus cloud formation. In this paper we focus attention on the connections between the observed vertical atmospheric structure, stratospheric–tropospheric aerosol content, and the resultant cirrus cloud properties. At

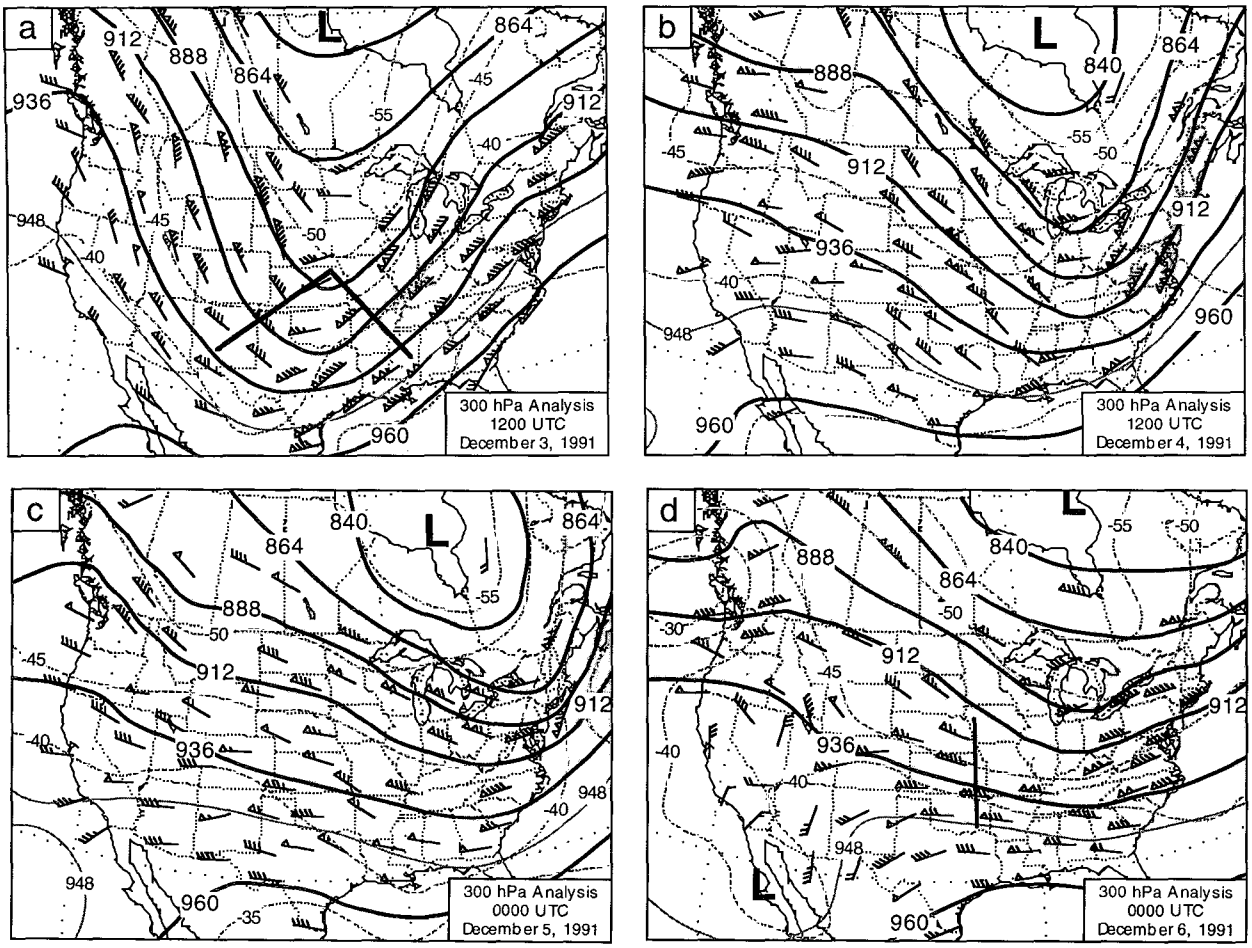

FIG. 1. 300-mb analyses constructed using conventional radiosonde data for (a) 1200 3 December, (b) 1200 4 December, (c) 0000 5 December, and (d) 0000 6 December. Solid lines are geopotential heights in 240-m intervals, thin stippled lines are isotherms at 5°C intervals, and light- and heavy-shaded areas correspond to 35–55 m s^{-1} and >75 m s^{-1} wind speeds, respectively. The thick solid lines in (a) and (d) denote the cross sections in Figs. 2 and 5, respectively.

the same time, the unique IFO II observing capabilities are highlighted. More detailed experimental and model findings will be given in subsequent case study papers.

2. The Intensive Field Observation II experiment

Unlike the IFO I that featured a mesoscale (~100 km) array of four lidar ground stations and often wide-ranging aircraft operations, the second field experiment emphasized aircraft missions that were closely coordinated with an extensively instrumented central Hub site at the Coffeyville airport (37.10°N, 95.58°W), along with two nearby (~20 km) remote sensing stations positioned along the expected mean cirrus cloud wind direction. This change in emphasis reflected the attitude that the benefits accrued by overlapping the instrument cloud coverage to yield synergistic multi-wavelength, multitechnique datasets outweighed any advantages of a more dispersed deployment, even given the spatial variability of cirrus cloud systems. A primary reason for the choice of this midwestern site was the availability of data from the initial installations of the developing National Weather Service (NWS) wind profiler network. These measurements provide highly useful dynamical information related to mesoscale cirrus cloud formation and were supplemented by special project wind profilers and rawinsonde (CLASS) soundings, as well as enhanced western to central regional NWS rawinsonde operations. A secondary purpose was to allow for the possible investigation of different types of cirrus than were studied during IFO I, including late-season convective anvil outbreaks and cirrus associated with subtropical jet streams.

The participating instrumentation supporting the Hub scientific objectives can be characterized as a model of modern research capabilities: three cloud microphysical–radiation aircraft, plus an overflying ER-

2 remote-sensing platform; four lidar systems encompassing polarization diversity, Raman, high spectral resolution, and infrared Doppler techniques; special sondes to measure vertical atmospheric structure, ozone, and ice crystal types; dedicated microwave wind and RASS temperature profilers; and an unparalleled variety of passive remote sensors, including the initial Spectral Radiation Experiment (SPECTRE) deployment (Ellingson et al. 1993). Since the full extent of these research capabilities will be illuminated in following IFO-II case study papers, only the specifications of the major instruments yielding available datasets pertinent to this research are outlined here.

The specifications and data quantities gathered by the Coffeyville Hub and ER-2 active remote sensors utilized here are listed in Table 1. These include the University of Utah Polarization Diversity Lidar (PDL), the NOAA Wave Propagation Laboratory CO_2 Doppler lidar (Post et al. 1992), the NASA Goddard Space Flight Center water vapor/nitrogen Raman (Whiteman et al. 1992) and downward-looking ER-2 polarization cloud lidar (CLS) systems, and the Pennsylvania State University W-band radar. A coaligned (PRT-5 type) narrowbeam (0.14°) midinfrared (9.5–11.5 μm) radiometer was also operated with the PDL unit to measure the effective atmospheric window brightness temperature of the clouds plus atmosphere. Also stationed at the Hub site was a developmental high spectral resolution lidar (HSRL) from the University of Wisconsin at Madison. The lidar systems at the two nearby ground sites were the University of Wisconsin volume imaging lidar (VIL—see Eloranta and Forrest 1992) and the NASA Langley Research Center polarization scanning lidar. In addition to the standard parameters of state and cloud microphysical instrumentation aboard the NCAR King Air and Saberliner and the University of North Dakota Citation aircraft, special cloud microphysical and aerosol sensors were deployed in order to focus attention on the nucleation mechanisms and the shapes of the cirrus particles (see Table 2).

3. Vertical atmospheric and aerosol structures

Over the case study period from 0000 (all times UTC) 5 December to 2400 6 December 1991, three separate occurrences of cirrus clouds were comprehensively studied from the Hub site. However, for the current purposes it is useful to begin our examination of the local atmospheric and aerosol vertical structures at 0000 3 December, just prior to the spectacular twilight observations on the evening of 3 December and dawn of 4 December. During the early portion of the case study period (0000 3 December–0000 5 December), the upper-tropospheric flow pattern over North America was dominated by a single high-amplitude trough–ridge system. As shown in Fig. 1a, at 1200 3 December a deep trough at 300 mb extended from a low near Hudson Bay though the central United States and into northern Mexico. A southwesterly jet stream with a speed maximum of 75 m s^{-1} extended from central Mexico into the Canadian Maritime Provinces, and a northwesterly jet (60 m s^{-1} maximum) reached from the Gulf of Alaska to the desert Southwest of the United States. Locally in southeastern Kansas, 3 December began as a cold dreary day, with frozen precipitation of various kinds giving way to a broken low-level cloud deck that dissipated before sunset.

Analysis of this system has been performed by compositing NWS rawinsonde data (processed at full vertical resolution), Project FIRE CLASS rawinsonde data, and NWS Wind Profiler Demonstration Network (WPDN) horizontal wind data. Figure 2 shows the thermodynamic and wind structure of the system along a cross section "folded" across the trough axis roughly normal to the axis of the jet stream (see Fig. 1a). An elevated frontal zone associated with the most intense region of cyclonic shear vorticity in the northwesterly jet extended from the trough axis southwestward. Isentropic potential vorticity (IPV) in this cross section exhibits a large discontinuity near the frontal interface extending down to near the 500-mb level. This feature

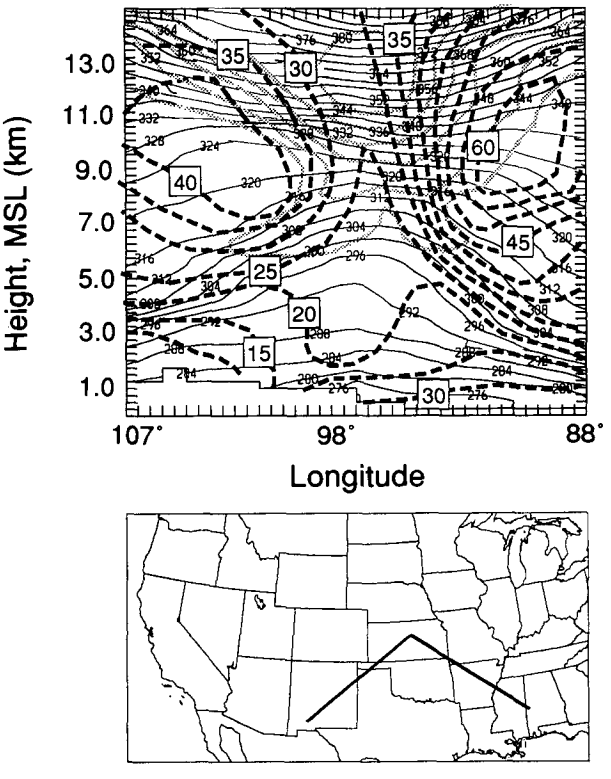

FIG. 2. Vertical cross section along the solid line segments in the map below and in Fig. 1a for 1200 UTC 3 December, centered around the upper-level trough axis. Contours are horizontal wind speed (heavy dashed lines) in m s^{-1} with an interval of 5 m s^{-1}, potential temperature (thin solid lines) at 2 K intervals, and isentropic potential vorticity (light solid lines), where the outer and inner contours are 100 and 600 ($\times$ 10^{-7} K mb^{-1} s^{-1}).

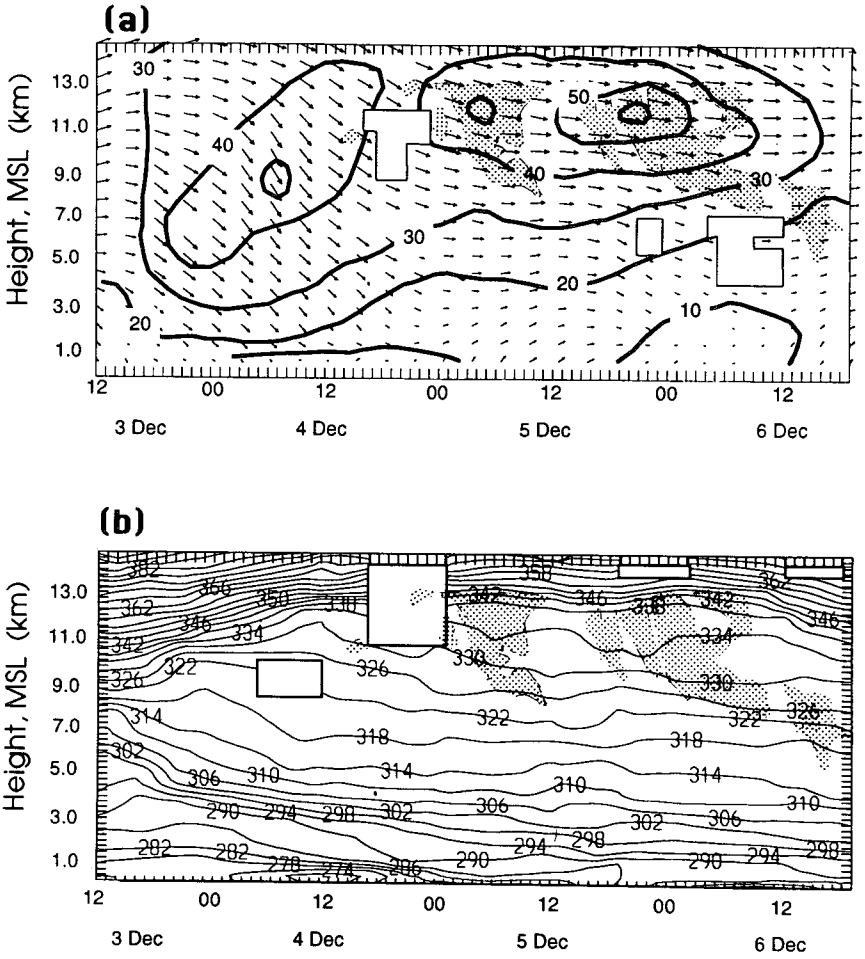

FIG. 3. Time–height cross sections of (a) horizontal wind velocity and (b) potential temperature over Coffeyville, Kansas, from 1200 3 December to 1800 6 December. (Rectangular blocks represent areas lacking sufficient data to complete the displays.) Stippling depicts the approximate cirrus cloud boundaries measured by the Hub remote sensors over the entire period.

has been shown to be indicative of an intrusion of stratospheric air into the middle and upper troposphere, otherwise known as a tropopause fold (Danielson 1968; Shapiro 1976), in association with intense upper-tropospheric baroclinic zones. Among other things, tropopause folds have been documented as a mechanism for injecting stratospheric aerosols of volcanic origin into the troposphere (Shapiro et al. 1984). Assuming that widespread enhanced aerosol loading existed in the lower stratosphere as a result of the Pinatubo eruptions (see below), it is not unlikely that stratospheric aerosols could have been deposited into the middle and upper troposphere over a large portion of the western and southwestern United States by this active fold event.

The spatial extent of the elevated frontal surface becomes evident in light of Fig. 3. These time–height cross sections of potential temperature and horizontal wind over Coffeyville show the elevated frontal surface in the northwesterly flow upstream of the trough axis for a 78-h period beginning 1200 3 December. The layer of enhanced static stability, defined by the 294 and 306 K isentropes, was continuously observed at lower levels with the passage of time and could still be recognized as a distinct entity 36 h later. Given a mean advective speed of 20 m s^{-1}, the longevity of this feature suggests an along-trajectory length scale of more than 2500 km. This illustrates the large geographical extent of this feature. Note that the boundaries of all cirrus clouds observed over this 4-day period by the Hub lidar and radar systems (see next section) are also shown as the stippled areas in these figures.

By 4 December (Fig. 1b), the jet–trough system had propagated eastward, resulting in a more zonal flow pattern over much of western North America. This process is also evident in the time–height cross sections shown in Fig. 3. Winds over Coffeyville veered from westerly to northwesterly from 1200 3 December to 1200 4 December, while the tropopause heights cor-

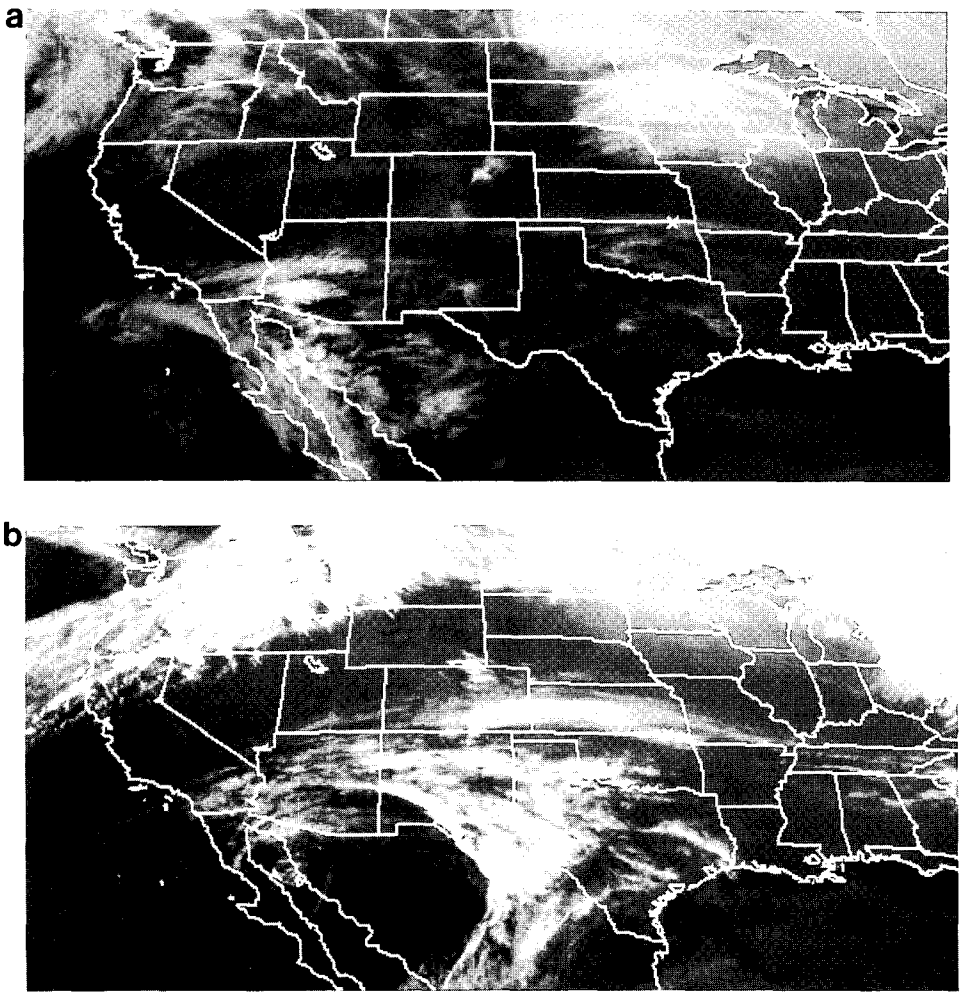

FIG. 4. Large-scale GOES satellite infrared imagery for (a) 0600 5 December and (b) 0000 6 December. The x symbol locates the Coffeyville site in southeastern Kansas. (Images courtesy of P. Minnis.)

respondingly increased from about 8 to 12 km. However, a closed low pressure system, which appears to have played a role in moisturizing the upper-tropospheric flow and the subsequent production of cirrus clouds over the southern Great Plains, began intensifying to the west of the Baja peninsula.

By 0000 5 December, a subtropical jet stream extended from the Four Corners region eastward along the Kansas–Oklahoma border (Fig. 1c). As depicted schematically in Fig. 3 and as shown in the satellite imagery of Fig. 4, cirrus clouds existed locally at and below the level of maximum wind along the anticyclonic shear side of the jet axis. The position of the cirrus relative to the upper-tropospheric flow is qualitatively in line with theoretical expectations of reduced static stability and upward motion below the level of maximum wind in the right-rear quadrant (i.e., entrance region) of a jet streak (Mattocks and Bleck 1986). Although the corresponding vertical cross-sectional analysis (not shown) failed to reveal local near-tropopause baroclinic zones or a "classic" fold event associated with this cirrus-generating feature (e.g., see Keyser and Shapiro 1986), there is a suggestion of a layer of enhanced static stability defined by the 318 and 326 K isentropes (Fig. 3) corresponding to the cirrus cloud-base region.

The thermodynamic and wind structure of the next jet streak (centered at 2000 5 December and 12.0 km over Coffeyville; Fig. 3a) was considerably more intense and better defined. The vertical cross section normal to the upper-tropospheric air flow at 0000 6 December (Fig. 5) reveals a weak elevated frontal zone bounded by the 320 and 328 K isentropes that is well correlated with the region of largest cyclonic shear vorticity associated with the jet streak. Corresponding values of isentropic potential vorticity depict a discontinuity from tropospheric to stratospheric values along the frontal interface that is strongly suggestive of a

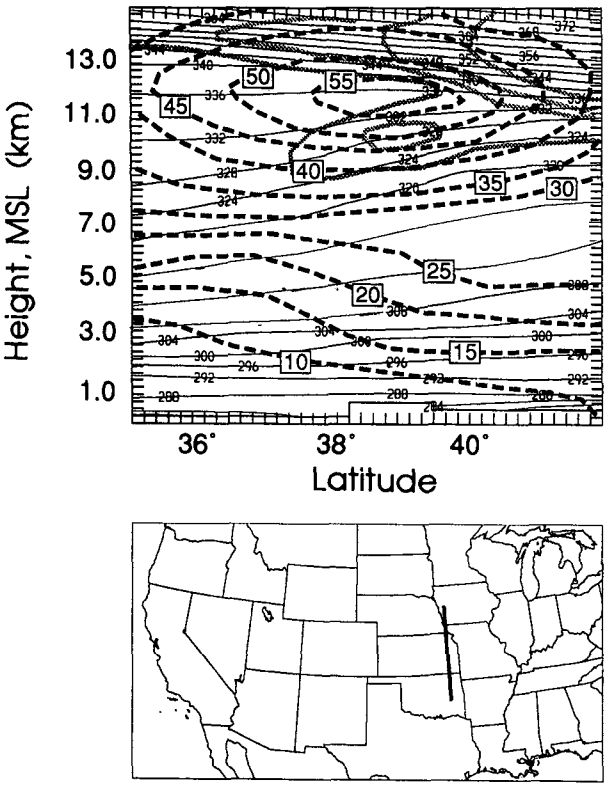

FIG. 5. As in Fig. 2 except for 0000 6 December along the heavy solid line segment depicted in Fig. 1d.

folded tropopause over central and northern Kansas. Satellite imagery (Fig. 4b) shows that the cirrus clouds observed during this period (see also Fig. 3) were part of an elongated shield of cirrus that extended eastward from the closed low near southern California (Fig. 1d), which appears to have been orographically enhanced over central Colorado. The base of the cirrus clouds observed over Coffeyville (~37°N) at this time was at 8.5 km with tops near 13 km. The lower cirrus layer height corresponds to the upper portion of the elevated frontal zone and the southern extent of the stratospheric potential vorticity in the cross section. Additionally, data from an ozonesonde launched at about this time (Fig. 6c) reveals a well-defined spike in the ozone profile centered at 8.75 km. Based on this analysis, we conclude that the cirrus observed over Coffeyville on the night of 6 December, and likely on 5 December as well, existed within a layer bounded from below by the elevated frontal surface and above by the tropopause, such that the cirrus clouds were in direct contact both with stratospheric air at the tropopause and with a layer of midtropospheric air of very recent stratospheric origin.

The layer of enhanced static stability attributed to this upper front continues to be evident in the potential temperature cross sections at 1200 6 December and 1800 6 December (not shown), although the frontal zone appears to be disconnected from the tropopause, and the IPV discontinuity is no longer clearly evident. This 6-hour period roughly brackets the third cirrus event of this case study.

Views of the changes in the stratospheric–volcanic aerosol scattering properties derived from the nocturnal Raman lidar measurements over the corresponding period are given in Figs. 7a–d (see also Ferrare et al. 1992). This data sequence reveals that the main body of the aerosol layer was present close to the bottom of the stratosphere over the period and also illustrates the relatively rapid height increase in the lower aerosol boundary over the night of 4 December in connection with the local deamplification of the upper-level pattern. The presence of upper-tropospheric cirrus clouds, which are at times only narrowly separated from the

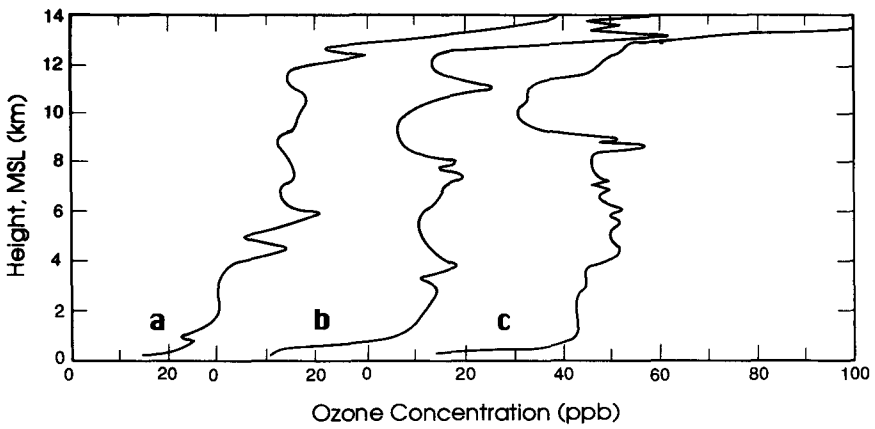

FIG. 6. Sequence of vertical ozone profiles (in parts per billion by volume) measured by ozonesondes launched daily at about 0000 on (a) 4, (b) 5, and (c) 6 December from Coffeyville, Kansas. Curves (b) and (c) are each shifted to the right by 30 ppb.

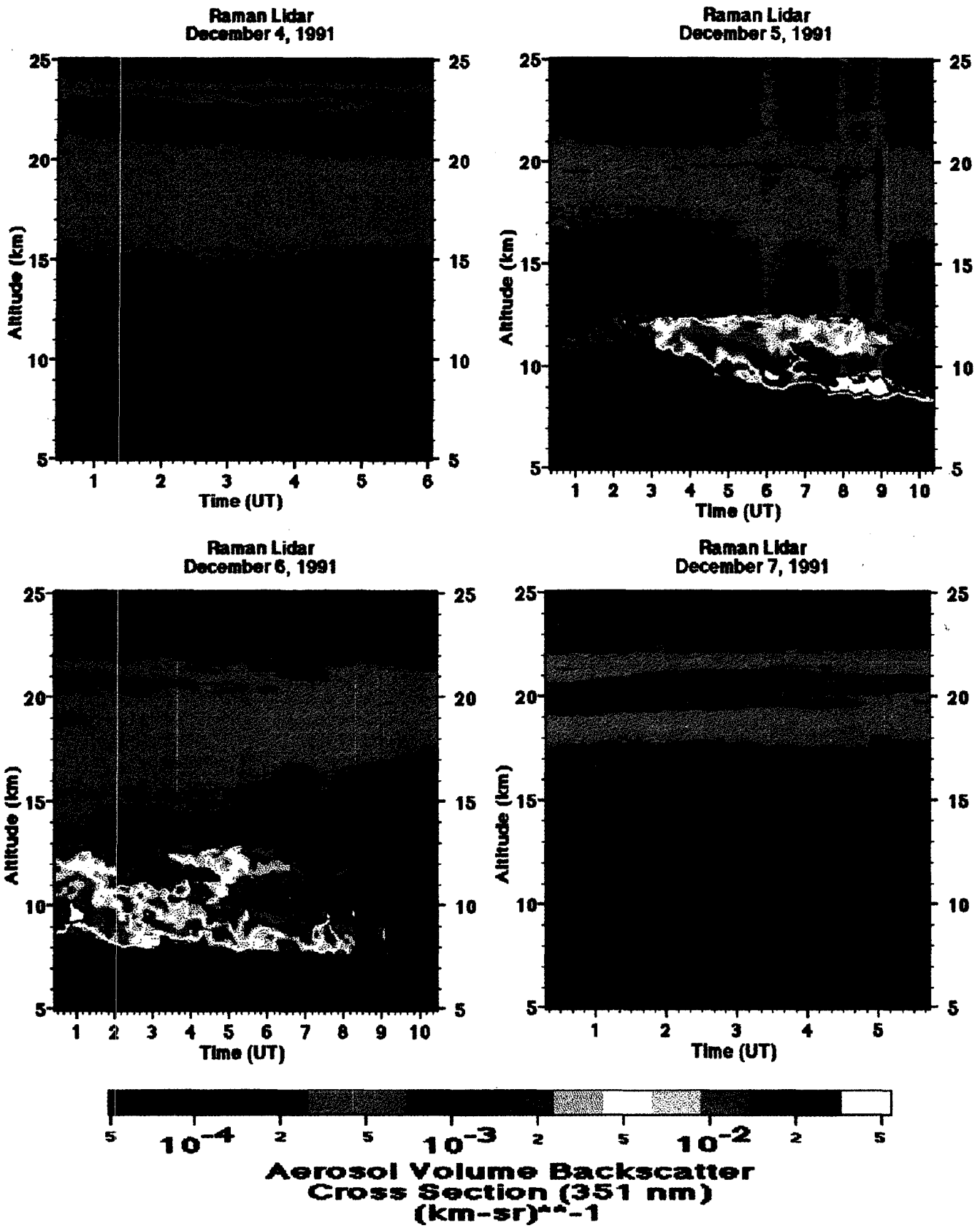
Raman Lidar
December 4, 1991
Raman Lidar
December 5, 1991
Raman Lidar
December 6, 1991
Raman Lidar
December 7, 1991
Altitude (km)
Time (UT)
10^-4
10^-3
10^-2
Aerosol Volume Backscatter
Cross Section (351 nm)
(km-sr)**-1

stratospheric volcanic aerosol layer, are also indicated in *b* and *c*. For comparison, time-averaged aerosol backscattering profiles derived from both day and night CO_2-lidar measurements bracketing the case study period are provided in Fig. 8. Although the backscattering properties of atmospheric aerosols at the laser wavelengths of 0.531 and 10.6 μm can differ, both lidars indicate similar temporal variations in the stratospheric aerosol. In addition, the CO_2-lidar data clearly show the major post-Pinatubo enhancement of tropospheric aerosols (Post et al. 1992), where the day to day aerosol variations between 8.0 and 13.0 km (i.e., in the cirrus cloud developmental region) are particularly significant. Finally, the 3-day sequence of local vertical ozone profiles in Fig. 6 also provides evidence for variable regions of enhanced ozone concentrations within the troposphere. These direct indications of stratospheric–tropospheric air exchanges suggest that a variety of upwind mixing processes were active in the upper air flow pattern that swept over the IFO II project area, even through only two tropopause folds were identified locally in our previous analyses.

In the following section, detailed cloud remote sensing and supporting in situ data are examined to investigate the possible effects of the jet streak dynamical processes on cirrus cloud formation and structure.

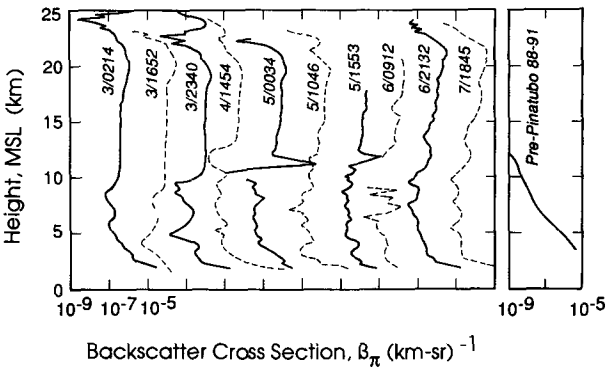

FIG. 8. Aerosol backscatter cross sections through the troposphere and lower stratosphere obtained at the 10.6-μm CO_2 lidar wavelength at the indicated day/time, illustrating the considerable extend and variability of volcanic aerosol content during the case study period (compare with the long-term average pre-Pinatubo profile obtained from Boulder, Colorado, at extreme right). (Note that the peaks near 11.5 km at 0034 and 1553 5 December are due to diffuse cirrus clouds.) Starting from the left, each profile is shifted by one division to the right.

4. Remote sensing and in situ cloud measurements

a. 0000–1000 5 December cirrus clouds

As can be seen schematically in Fig. 3, although thin scattered cirrus clouds began to make their initial appearance by midday on 4 December, it was not until the arrival of the jet streak after sunset that local cirrus cloud development became significant (Fig. 4). The passage of this cirrus streak is illustrated in Fig. 9, with PDL time–height displays of range-normalized returned power (P) and linear depolarization ratio (δ, the ratio of the cross to parallel polarized signals returned from the vertically polarized laser pulse) and coaligned narrowbeam midinfrared radiometer atmospheric brightness temperature T_{eff}. As is also apparent in the lower-resolution Raman lidar data (Fig. 7b), the most long-lived feature of this cloud system was a diffuse tropopause-topped cirrus layer, which sporadically increased in vertical extent through the action of fallstreaks, only to subsequently fade back to near the tropopause. During its most active precipitating stage at ~0600, however, this layer appears to have spawned a convective cirrus cloud layer ranging in height from 8.5 to 9.5 km. Prior cirrus research suggests that a conditioning of subcloud air through precipitation and evaporation processes can lead to this result (Starr and Cox 1985; Sassen et al. 1990). The NASA Raman water vapor data in this case (Fig. 10) confirm a gradual downward sloping moistening of a dry layer from about 7.0–9.0 km (possibly representing an elevated frontal zone).

The lower cirrus layer, on the other hand, produced considerably stronger laser backscattering, which was at times highly depolarized, and can be associated with the highest measured values of T_{eff}. As shown in the top panel of Fig. 9, T_{eff} gradually increased from the atmospheric background temperature of −70°C to −60°C at about 0600 (i.e., until the lower cirrus layer started to become established). Thereafter, even as the upper layer diminished in thickness, T_{eff} approached −40°C on two occasions (~0750 and 0850) when relatively deep and strongly scattering fallstreaks developed in the trailing cirrus layer. Higher-resolution details of the lower cloud structures are provided in Fig. 11, where a series of convective ice-phase uncinus cells ($\delta \approx 0.45$) with trailing crystal fallstreaks are found in (a), a strongly scattering region displaying a fine structure of mammatus-like protrusions and a highly depolarizing ($\delta = 0.6$–0.7) cloud-top region in (b), and in (c) is shown a highly supercooled (~ −35°C) liquid-phase altocumulus cloud ($\delta \leq 0.05$) that developed just below the cirrus cloud trailing edge (apparently in re-

FIG. 7. Raman lidar height–time displays of volume backscatter cross sections (km sr)$^{-1}$ in the 0.351-μm aerosol channel, collected over the indicated times on the consecutive nights of 4–7 December [(a)–(d), respectively]. The logarithmic backscatter scale (inserted at bottom) was chosen to characterize both the volcanic aerosol content and the generally diffuse upper-tropospheric cirrus clouds present on the nights of 5 and 6 December. Note that the vertical stripes above the cirrus clouds in (b) are due to detector noise associated with the strong signal attenuation produced by regions of the cloud layer.

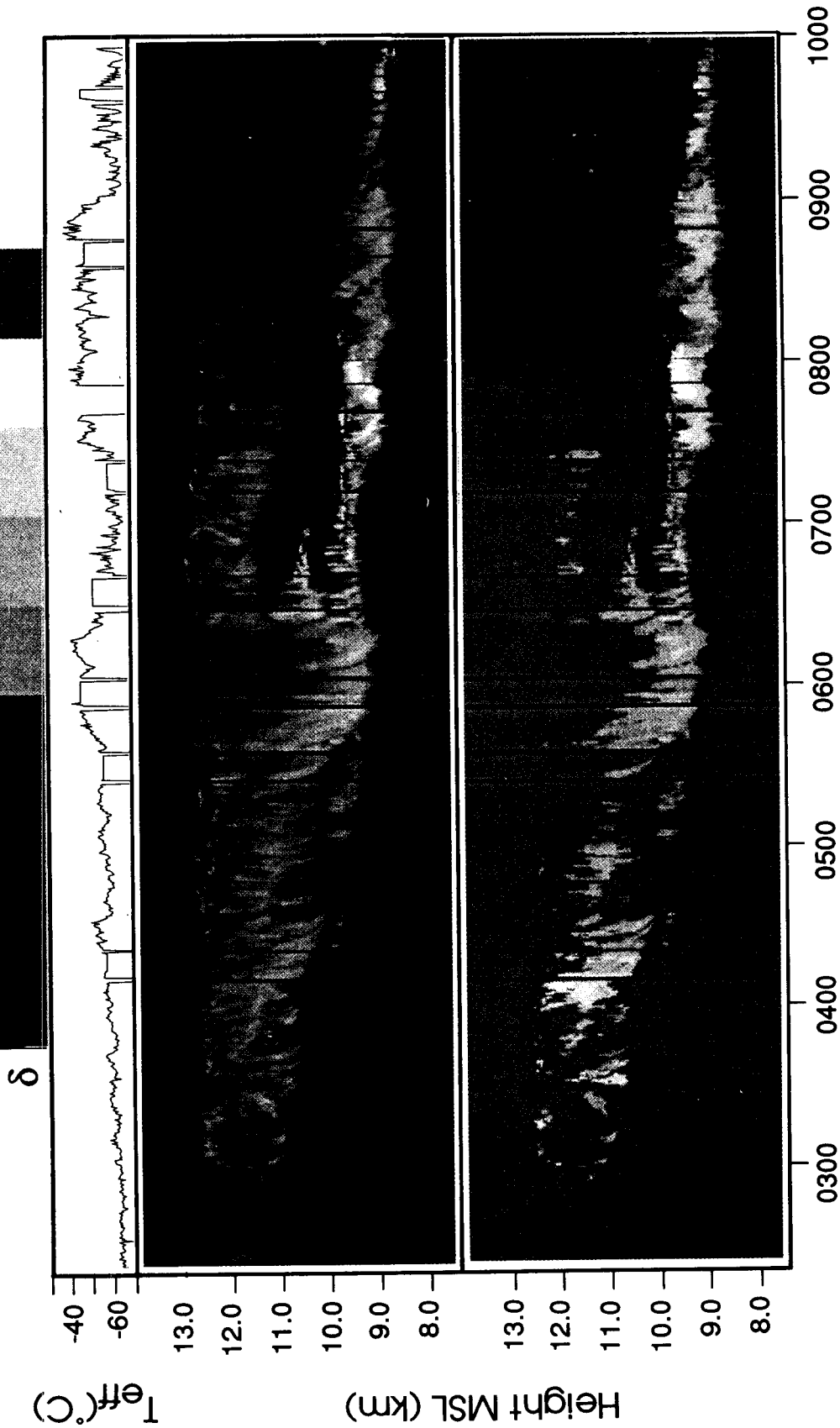

FIG. 9. Polarization lidar HTI display of relative range-normalized backscattered power P (top, based on a logarithmic grayscale) and linear depolarization ratios (bottom, see δ key at top) of the cirrus clouds studied on the night of 5 December. The panel at top provides the effective atmospheric window infrared brightness temperatures T_{eff} measured by a coaligned narrowbeam radiometer (except during the intermittent 10-Hz PDL data files, where frequent recording errors occurred). Note that the δ value display is incomplete because noise- or molecular scattering–dominated signals are rejected during analysis (and assigned the middle-gray background shown at the right end of the δ-value key).

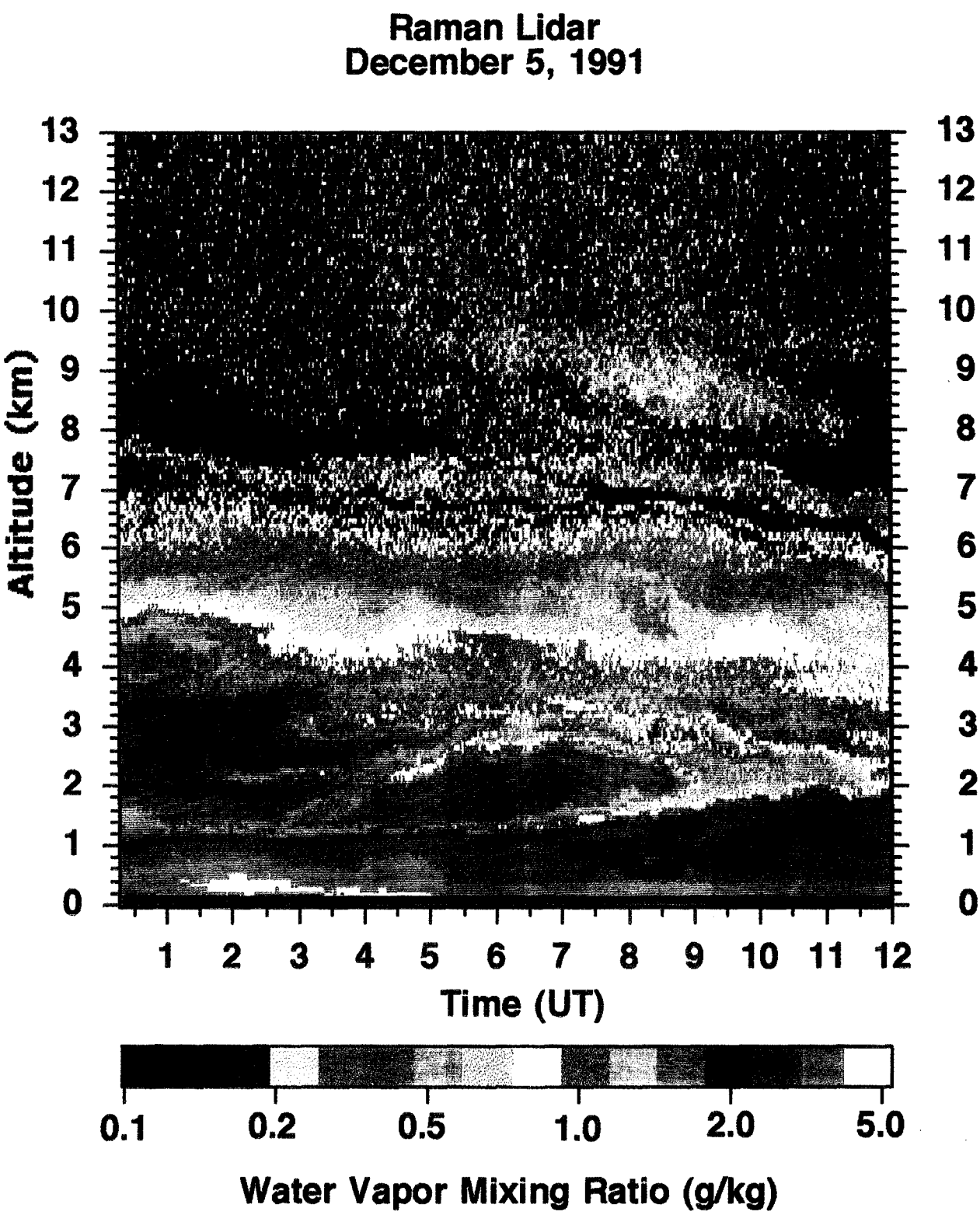

FIG. 10. Raman lidar HTI display of water vapor mixing ratio in g kg^{-1} (see key at bottom) on the night of 5 December. Note the descending layer of humidity just below the cirrus cloud, which produced sufficient attenuation to generate the erroneous signals above ~10 km. Considerable boundary-layer water vapor structure is present.

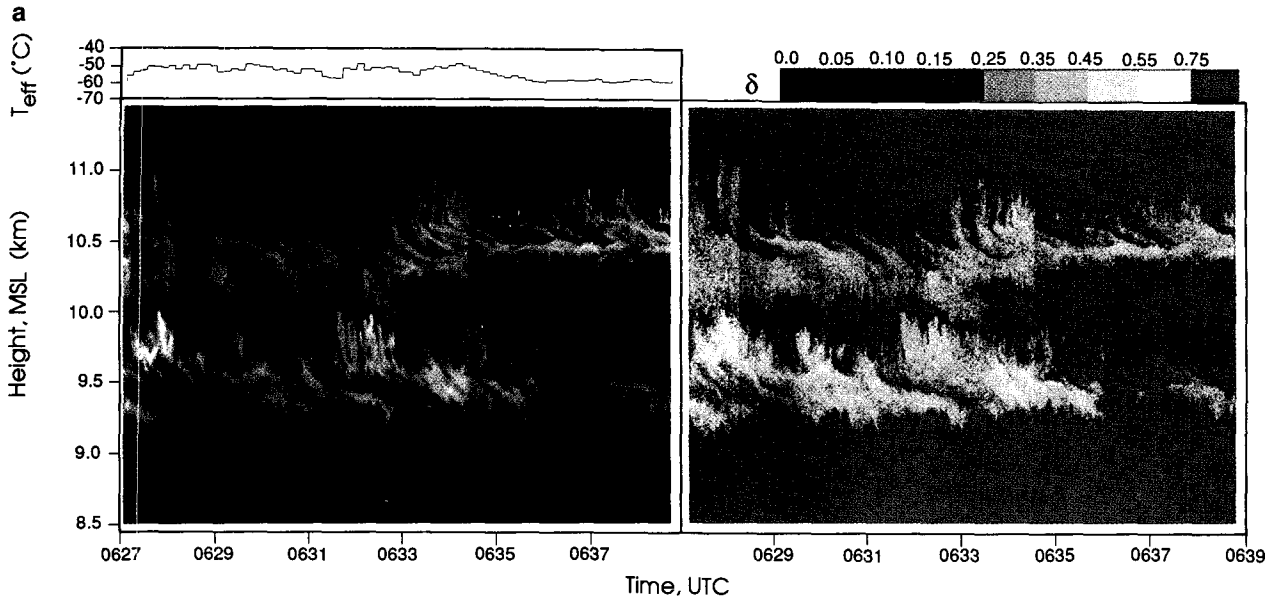

FIG. 11. High resolution height–time PDL displays of relative returned energy and depolarization (right of each pair) illustrating the highly structured convective lower cirrus layer at the indicated times on 5 December. Shown in (a) are numerous sheared fallstreaks emanating from two layers of uncinus cells, (b) a dense and highly depolarizing region above mammatus-like structures, and (c) the brief appearance of a highly supercooled altocumulus ($\delta \leq 0.05$) cloud just below the trailing edge of the cirrus cloud base.

sponse to the humidification caused by prior cirrus particle evaporation), only to be disrupted by plumes of ice crystals resulting from cirrus particle-seeding effects. Note that values of T_{eff} are relatively high in the deep fallstreaks of (a) and (b) and much lower in the dissipating cirrus cloud trail in (c), although the passage of the supercooled altocumulus cloud seems to have caused a small increase in effective temperature. Views such as these illustrate that it is the accumulation of cirrus uncinus fallstreaks that often defines the base of a cirrus cloud layer (see Sassen et al. 1990).

A Citation aircraft mission, involving racetrack patterns 10–15 km long and an Eulerian spiral descent was conducted in close support of the Hub site from 0612–0847. (The excellent aircraft navigation was confirmed by the sighting of the green PDL laser beam at one point just off the wing tip over the Hub!) Figure 12, which superimposes the corrected aircraft altitude flight pattern on an expanded PDL lidar returned power display, reveals that the platform sampled both the tenuous upper and denser lower layers. The corresponding time plots of aircraft air T and dewpoint T_d temperatures, 2D-C probe ice particle mean size d and concentration N_i, and condensation nuclei CN and ozone concentrations are provided in the panels below the lidar display. Note that the cirrus precipitation-induced humidification of the subcloud region shown by the Raman water vapor profiles (Fig. 10) is also indicated by the differences in the dewpoint measurements at ~9.0 km obtained during the ascent and later descent legs through the developing lower cirrus cloud layer. The in situ and remote cloud measurements are generally in quite good agreement in defining the cirrus cloud boundaries, although strong optical attenuation in the developing lower layer partially blocked the probing of the upper layer at those times corresponding to the highest observed T_{eff} values (see top panel of Fig. 11b). The combined evidence shows that the two cloud layers have dissimilar microstructures, with the higher cirrus displaying much lower ice crystal concentrations and different crystal shapes (according to the lidar δ values). In addition, at cloud top at 0751, FSSP particle concentrations (not shown) of ~0.2 cm^{-3} are found without any indications of ice crystals at a temperature of −64°C, indicating quite small ice or haze particles. The 2D-C probe ice crystal concentrations in the lower cloud often reach 200 L^{-1} and actually peak at ~600 L^{-1} (2-s averages are given in Fig. 12), which represents the highest value by far measured by any aircraft during the campaign (or elsewhere to the best of our knowledge). The photomicrograph examples of ice particles captured by a Formvar replicator device from 0800 to 0815 given in Fig. 13 indicate complicated radial particle shapes (that were generally too fragile to survive impaction intact), which can be said to be in keeping with the strong laser depolarization ($\delta \approx 0.65$) noted at this time and altitude (see Fig. 11b).

The variations in CN counts and ozone concentrations in the bottom panel of Fig. 12 have important implications for these unusual cirrus cloud properties. We provide these data in Fig. 14 in terms of vertical

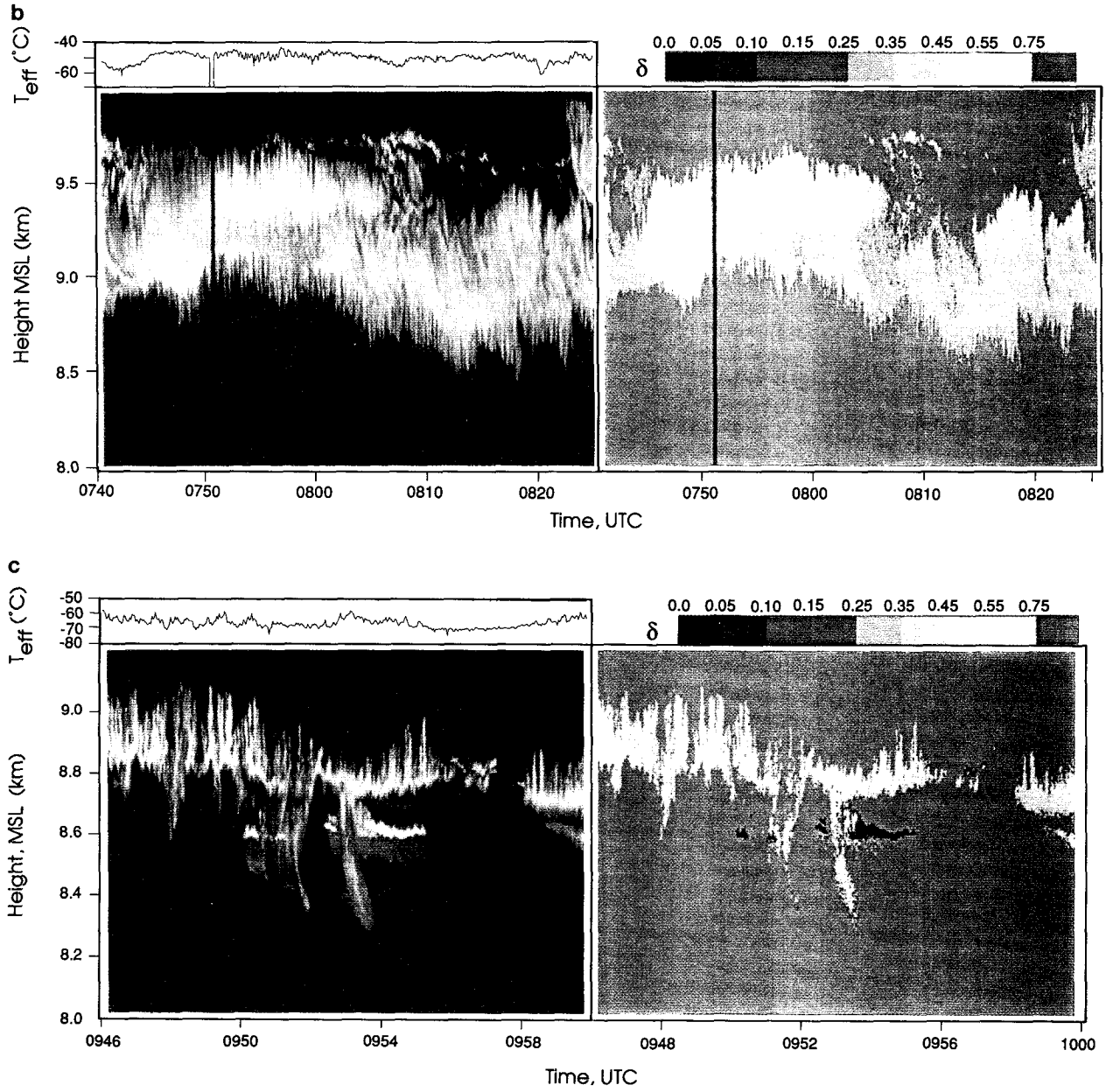

profiles obtained during the ascent (0612–0750) and descent (0751–0847) portions of the flight. It is apparent that CN counts are significantly enhanced in the height interval 7.0–11.0 km encompassing the lower cirrus cloud layer, with offscale counts of >1000 cm^{-3} at ~9.0 km present during the descent spiral. Figure 15 more directly illustrates the association of the high ice crystal concentrations with the upper portion of the aerosol layer. The ozone profiles (Fig. 14) tend to dip in the layer containing the greatest CN counts, but they also show increased concentrations of >20 ppb toward the top of the elevated aerosol layer. While the ascent and descent ozone profiles are similar, and are comparable to Fig. 6b data, those for the CN are sufficiently different to suggest considerable spatial variability in the aerosol distribution. (Note also the significant CN variations along the nearly level flight segment in Fig. 12 from 0805–0830.) In summary, the evidence presented here and in section 3 indicates an association between the formation and maintenance of the lower cirrus layer with the cirrus particle evaporation-induced humidification of a region containing elevated ozone

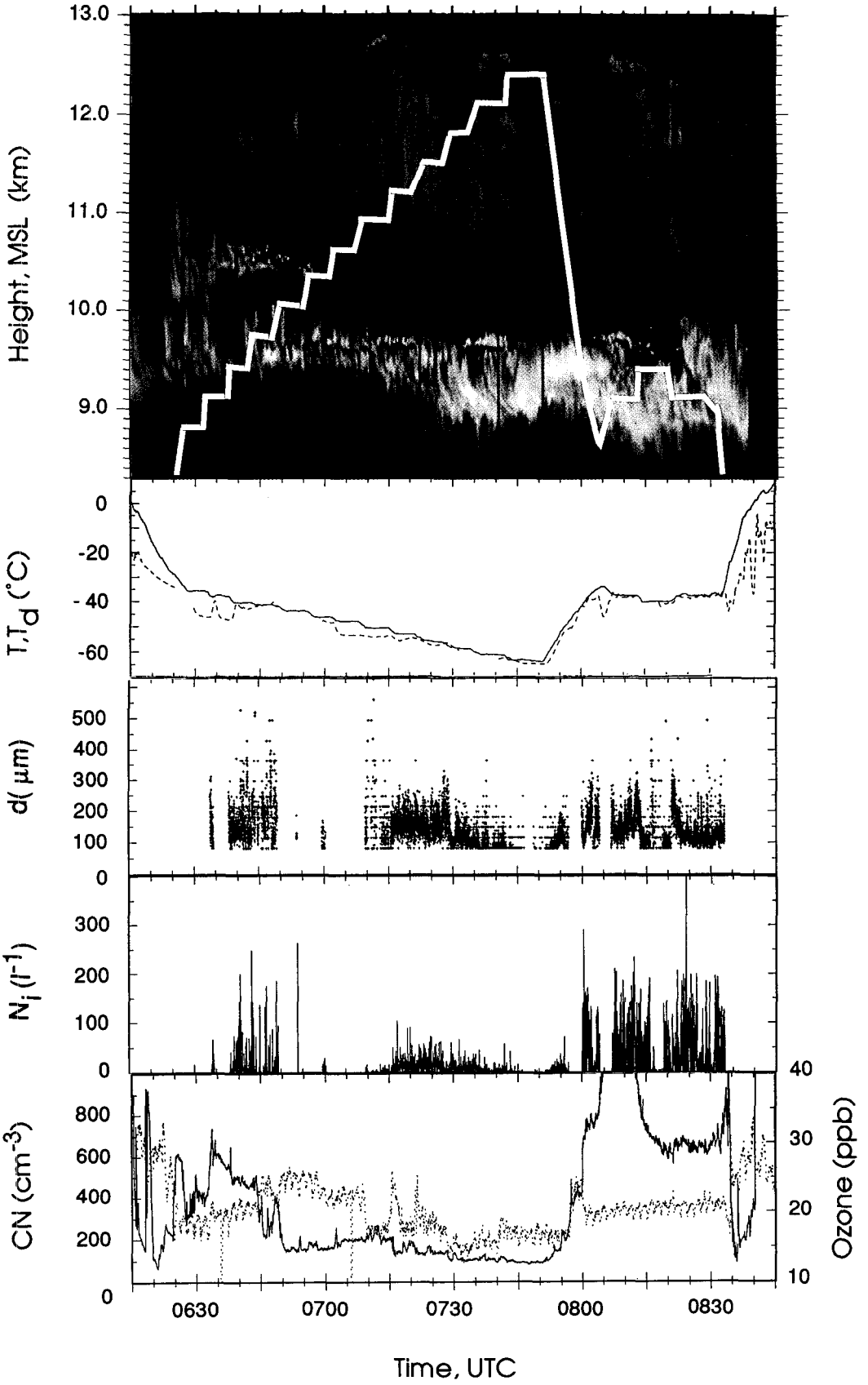
Height, MSL (km)
13.0
12.0
11.0
10.0
9.0
T,T_d (°C)
0
-20
-40
-60
d(μm)
500
400
300
200
100
0
N_i (l^-1)
300
200
100
0
CN (cm^-3)
800
600
400
200
0
40
30
20
10
Ozone (ppb)
0630
0700
0730
0800
0830
Time, UTC

and aerosol concentrations of probable stratospheric origin.

b. 1800 5 December–0800 6 December cirrus clouds

A number of airborne missions in the vicinity of the Hub were conducted early during this period as thin cirrus clouds initially made their appearance, but generally the missions were performed prior to the local occurrence of the deep jet streak cirrus cloud band (see Figs. 3 and 4). We again utilize Citation measurements from a mission featuring a step pattern between the Hub and Parsons (30 km to the northeast) sites from 1756 to 2023 5 December. In addition, downward-looking lidar data from the ER-2 platform obtained during a transit from Coffeyville to the Texas Gulf region are presented, since this dataset uniquely portrays the large-scale geographical distribution of volcanic aerosols (below the 20-km flight altitude) at ~2000 corresponding to the approximate time of the local jet maximum. Specialized aerosol measurements collected by the NCAR Saberliner are also given to further explore the issue of the nature of the aerosol.

The Citation data plots in Fig. 16 provide the same information as in Fig. 14, showing the height dependencies in CN and ozone concentrations during the ascent and descent legs. (Since zenith-pointing lidar data for this mission are incomplete, a combined display as in Fig. 12 is not available.) As in the previous Citation mission, greatly enhanced CN counts are found in the altitude interval 7.5–10.0 km, and Fig. 17 shows that the cirrus cloud region is again associated with the top of the aerosol-enriched layer. Moreover, thin strongly enriched aerosol layers between 10.2 and 12.2 km are embedded in the upper cirrus. Ozone concentrations (Fig. 16) display peaks near the main aerosol layer base and top, as well as near the Citation ceiling altitude, where it appears that ozone just above the tropopause was sampled. Additional aerosol information derived from the University of Missouri/Rolla mobile aerosol sampling system (as described in Hagen et al. 1992) during overlapping Saberliner missions is included in Table 3. These samples were taken below the cirrus cloud base in relatively dry air with relative humidities of ~25%: the average aerosol total mass (derived from four size distribution measurements and assuming unit density) was 0.1 μg m^{-3}. Of the three measurements of aerosol-soluble mass fraction (assuming the presence of either ammonium sulfate R_{AMS} or sulfuric acid $R_{H_2SO_4}$) obtained within the aerosol layer (compare sample heights with Fig. 16), one is significantly elevated (R_{AMS} = 0.22) above the usual tropospheric values of a few percent or less. The lower soluble mass fractions are consistent with previous measurements made in the altitude range 7.0–10.0 km over the central United States using bag samples processed in a laboratory-based continuous flow thermal diffusion chamber facility (Hagen et al. 1990). The measurement exhibiting the highest soluble mass fraction may suggest aerosols resulting from volcanic activity, or perhaps may be of aircraft exhaust origin.

The ER-2 CLS height-distance display of Fig. 18 covers 640 km of lower stratospheric and tropospheric aerosol and cloud returns along a north–south flight track at ~95°W latitude from Coffeyville (left) to near Houston, Texas. Note that the atmospheric cross section in Fig. 5 corresponds to a portion of this flight track and reveals the relationship between the high altitude aerosols and clouds (colored blue and white, respectively) and the vigorous jet streak defined by the 0000 6 December synoptic analysis. The lidar aerosol backscatter (at 0.53-μm wavelength) illustrates the enrichment of aerosols at the base of the stratosphere caused by the jet stream circulation. This is a powerful representation of the vertical and latitudinal redistribution of volcanic aerosols from the tropical belt into which the debris were originally injected. The wedged-shaped region of enhanced aerosols extending just above the gradually lowering surface of the tropopause (from 17.0 to 15.5 km, center to left) appears to be tenuously connected to the higher stratospheric aerosol layer at a distance of ~500 km (not shown) and also appears to slope downward toward the cirrus cloud tops ("overexposed" white regions in this image to highlight aerosol scattering) about 150 km north of Coffeyville.

The subsequent local development of the jet streak cirrus band (see Fig. 4b for satellite view) is traced in the PDL height–time returned power and δ displays of Fig. 19. Based on a 6-year lidar record of Project FIRE Extended Time Observations (ETO) of cirrus clouds collected at Salt Lake City, Utah, such complex cirrus structures containing an abundance of generating features within swirling layers are quite unusual. Effective infrared window brightness temperatures (top panel) are correspondingly variable in response to the variations in total physical cloud thickness and the accumulations of fallstreak particles. Sometimes $T_{eff} \approx -35$°C are encountered. Also, in contrast to the displays of Fig. 9, unusually high δ values are now sometimes found in generating areas in the usually diffuse upper cirrus regions. Moreover, the sporadic occurrence of low δ ($\lesssim$0.15) values in association with the

FIG. 12. Combined PDL lidar and University of North Dakota Citation aircraft data displays from the mission in support of the Hub remote sensors on the night of 5 December. At top is a height–time display of returned energy, with the Citation flight track shown superimposed in white, in situ data panels of air T and dewpoint temperature T_d (dashed), ice crystal mean diameter d and concentration N_i (derived from the 2D-C probe), and condensation nuclei CN and ozone (dashed, in parts per billion by volume) concentrations.

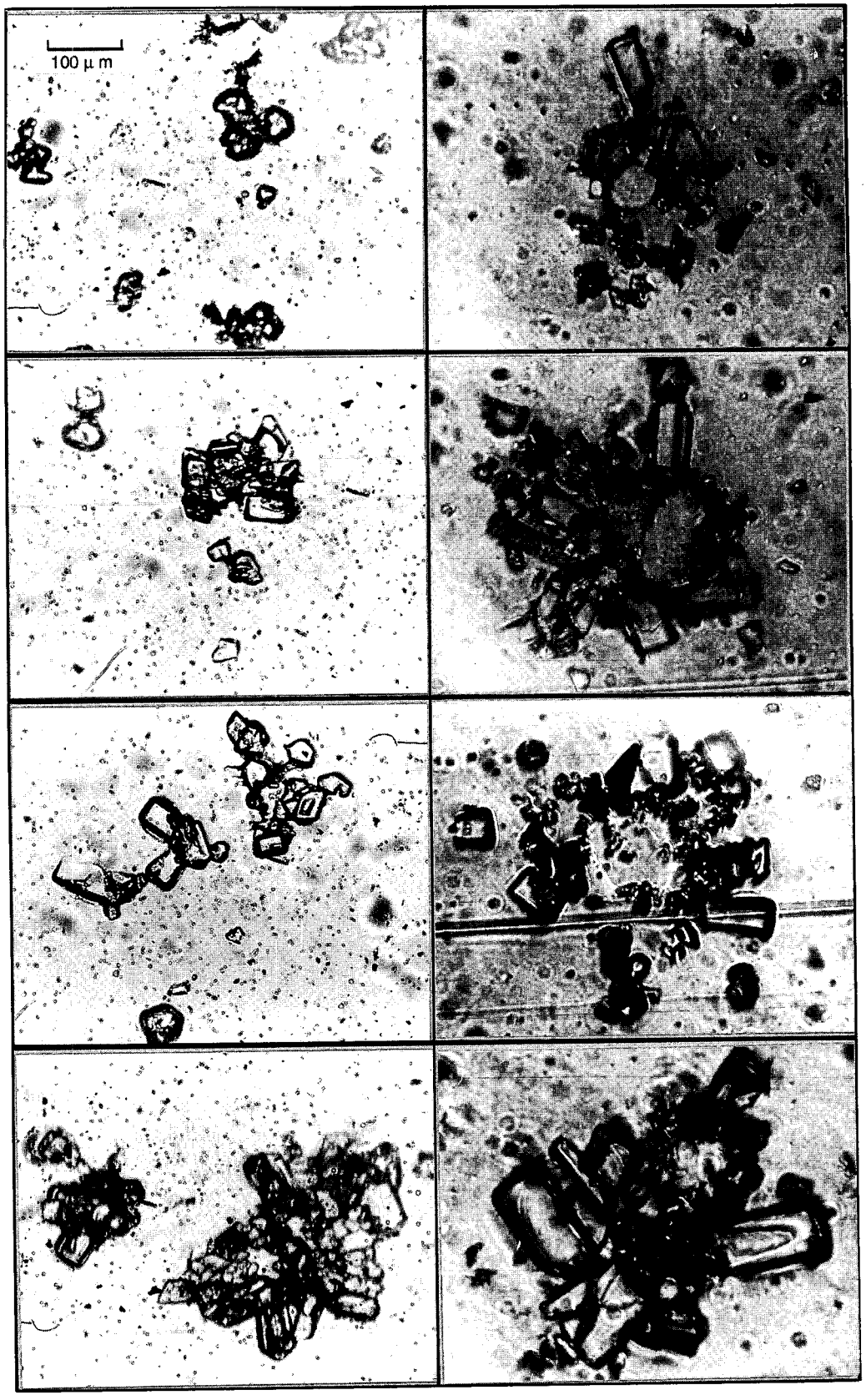
100 μ m

lower cirrus generating regions (at and below about 10.5 km) indicate the effects of spherical scatterers that appear to be intimately involved in the generation of the cirrus particle fallstreaks defining the cirrus cloud base. Given in Fig. 20 are higher-resolution displays of three such regions, which clearly identify the Mie scattering effects of rapidly growing haze particles in generating cell heads (Sassen 1992), despite the extremely low temperatures approaching −50°C (see figure caption). Although in the infrared window region the verniers of haze particles do not appear to have provided T_{eff} signatures (Fig. 20c), certainly the accumulations of ice crystals nucleated from them are associated with sufficient mass to significantly increase the T_{eff} produced by the entire depth of the cloud layer (Figs. 20a–b).

It is interesting to note that supercooled sulfuric acid droplets at temperatures as low as −48°C have been reported on the basis of in situ measurements in regions of the upper troposphere likely affected by tropopause folds (Yamato and Ono 1989). Comparison with the in situ CN profiles obtained earlier strongly suggest that these cirrus cloud features are the result of contamination from relatively large cloud-forming nuclei of volcanic origin. Although the low δ-value cell-top generating structures were not consistently observed, their association with crystal fallstreaks, which are long-lived, suggest their great importance to the formation and maintenance of the lower cirrus layer.

c. *1200–1700 6 December cirrus clouds*

The properties of the final cirrus cloud system of the case study period differ sharply from those described above, although Fig. 3 suggests that this relatively low-level cirrus (or altostratus) cloud mass represents a continuation of the precipitating cloud trail of the cirrus described above. The structure of this cirrus mass is best represented in the W-band (3.2-mm wavelength) PSU radar height–time display of Fig. 21, because this optically thick cloud, along with some lower stratus clouds, often produced strong optical attenuation of the lidar signals. This radar cloud image shows a succession of ice crystal fallstreaks emanating from generating cells at an altitude ~9.0 km, generally producing echoes significantly stronger and lower than those measured earlier.

Although the radar echo cloud-top heights lie close to the peak of enhanced CN counts measured ~20 h earlier by the Citation, more contemporaneous aerosol data are available from the NCAR Saberliner Hub mission from 1430 to 1630, in which CCN concentrations were measured by the University of Missouri/Rolla CCN counter. CCN counts in excess of 300 cm^{-3} were obtained throughout the cloud layer from 6.0 to 9.0 km, but at an altitude of ~7 km the number exceeded 1000 cm^{-3}. The significance to cloud formation of this great concentration of cloud-forming particles was subsequently revealed by the volume imager lidar (VIL) scans given in Fig. 22. Although these west–east VIL scans portray the cloud conditions only in the vicinity of the Hub (~11 km to the northeast of the VIL site), the scans reveal the presence of strongly attenuating cirrus or altostratus (Fig. 22a, left) and supercooled liquid altocumulus cloud layers, which were initially found embedded in the ice clouds (Fig. 22a, right) and later, alone, produced streaks of ice virga (Fig. 22b, right). Polarization lidar and aircraft measurements over the Hub confirm the predominantly liquid cloud phase of the altocumulus, which at an altitude of ~7.0 km corresponds to the peak in the CCN concentration profile measured by the Saberliner.

5. Discussion

We have provided indirect evidence for cirrus cloud formation and maintenance processes contaminated by relatively abundant volcanic cloud-forming nuclei, but fundamental questions must be addressed to justify this linkage between sulfur-based aerosols of stratospheric origin and cirrus cloud microphysics. Fortunately, recent research has already produced the framework to evaluate this interplay of rather exotic cloud processes. These studies include polarization lidar measurements of lower stratospheric volcanic aerosols and tropopause-topped corona-producing cirrus clouds, laboratory aerosol scattering simulations, and numerical model findings concerning the basic nature of cirrus particle nucleation at temperatures typical of the upper troposphere.

Two pathways from sulfuric acid droplet aerosol to cirrus cloud ice crystal have recently received experimental and theoretical attention. Although in either case it is unknown whether the stratospheric aerosol can serve as an efficient heterogeneous ice nuclei, cloud modeling evidence (Heymsfield and Sabin 1989; Sassen and Dodd 1989) has illustrated that at temperatures colder than −35° to −40°C the homogeneous freezing of solution droplets growing in updrafts likely represents an effective process to generate ice crystals. In

FIG. 13. Sequence of photomicrographs of Formvar-preserved ice crystals obtained from the Citation during the traverse of the lower cirrus cloud layer (see Fig. 12). The crystals at left were collected at a temperature of ~ −40°C from 0800–0802 as the aircraft first penetrated the cloud top, while those at right at −37.7°C from 0818–0820 during a leg at 9.45 km. These complex column/sector radial crystals generated the unusually strong laser depolarization shown in Fig. 11b. The cause of the unusual impacted-particle ringed structures, particularly evident at right, is uncertain. A 100-μm scale is inserted at top left for reference.

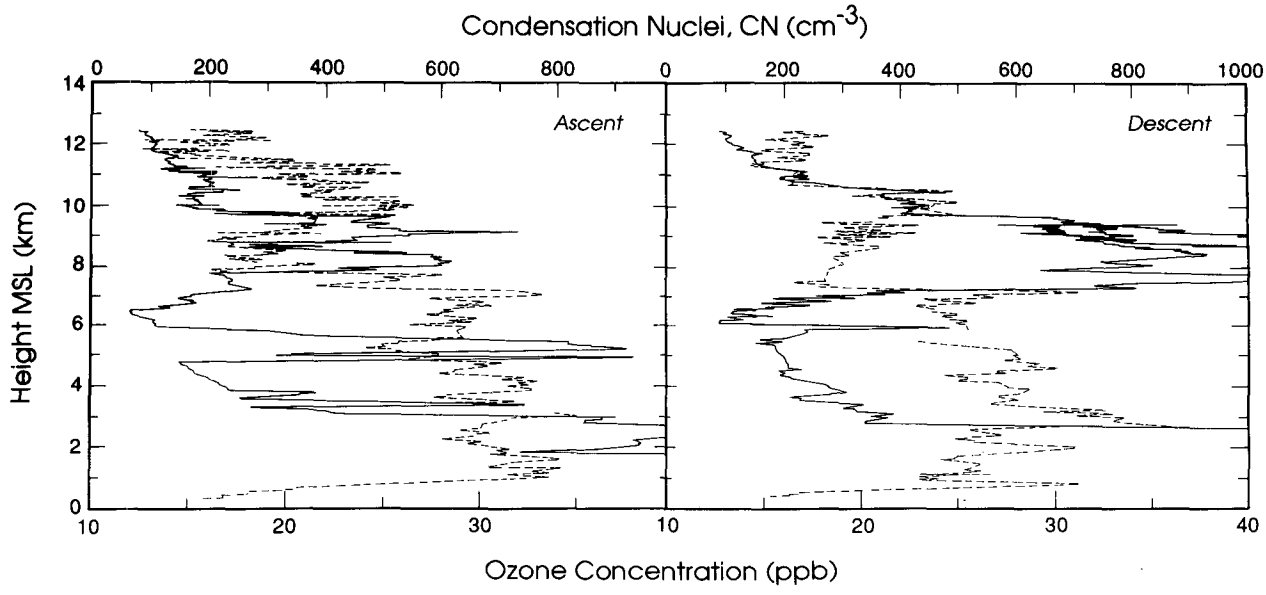

FIG. 14. Comparison of vertical profiles of condensation nuclei and ozone (dashed) concentrations measured by the Citation during the ascent (left) and descent portions of the Hub mission on the night of 5 December.

dealing with an aerosol of stratospheric origin either under background (e.g., see Friend et al. 1973; Bigg 1975) or volcanically perturbed conditions, the sulfuric acid droplets can either directly or indirectly participate in the ice nucleation process after tropospheric alteration. Evidence for the direct homogeneous freezing of sulfuric acid droplets, following a dilution in solution strength from water vapor diffusional growth in the vicinity of the tropopause, comes from polarization lidar studies of corona-producing cirrus clouds (Sassen 1991). These high cold clouds of relatively small (10–30 μm) particles produce relatively strong ($\delta \approx 0.55$–0.75) laser depolarization, indicative of complexly shaped ice crystals. Presumably these are radial particles that have a polycrystalline structure due to the effects of the coating of liquid sulfuric acid, which is excluded to the surface of the ice germ during drop freezing under the observed environmental conditions (Th. Peter 1992, personal communication).

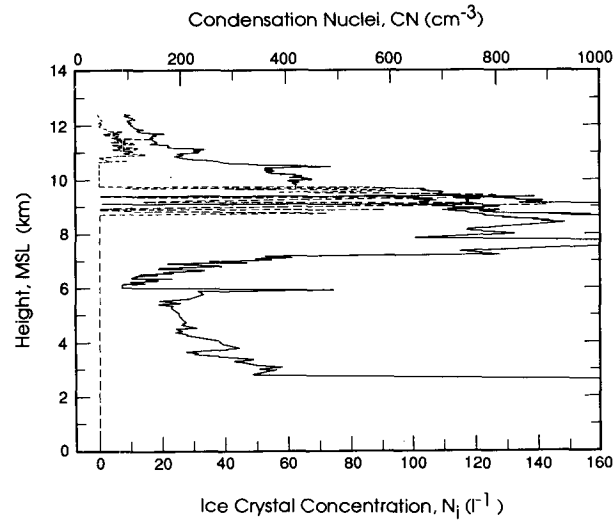

FIG. 15. Vertical profiles of 2D-C probe ice crystal (dashed) and condensation nuclei concentrations obtained during the Citation descent spiral over the Hub from 0753–0804 5 December, illustrating the connection between the cirrus particles and the elevated CN counts near the top of the aerosol layer.

The indirect path from sulfuric acid droplet to ice crystal involves the homogeneous freezing of haze particles formed on ammonium sulfate cloud condensation nuclei CCN that were derived from acid droplets. The chemistry of this process leading to the neutralization of the acid solution readily follows when droplets, especially if they are evaporating, are exposed to ammonia gas to produce ammonium sulfate crystals (e.g., see Rubel and Gentry 1985). Since ammonia gas is generated at the earth's surface primarily through biological activity (Georgii and Müller 1974) and is consumed photochemically in the stratosphere, this CCN creation process could become significant within tropopause folds where the ammonia gas enhancement of stratospheric air would favor ammonium sulfate CCN production. In support of this view, polarization lidar studies of an unusual lower-stratospheric volcanic aerosol plume affected by tropopause folding activity (Sassen and Horel 1990) yielded depolarization values consistent with partially crystallized sulfuric acid droplets created in the laboratory (Sassen et al. 1989). However, since sufficient time and ammonia gas concentrations may not be available to completely neu-

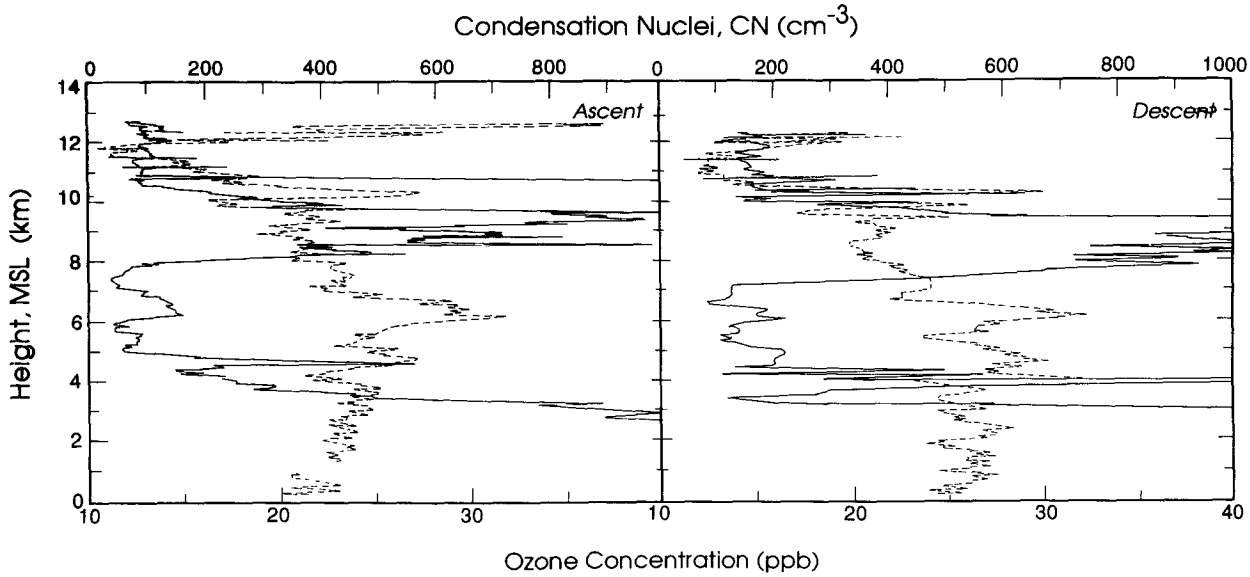

FIG. 16. Comparison, as in Fig. 14, of vertical profiles of CN and ozone (dashed) concentrations obtained during the ascent (left) and descent flight segments of the Citation mission of the afternoon of 5 December.

tralize the acid droplet population, it remains ambiguous which solution droplet freezing process would dominate cirrus cloud particle production following the type of stratospheric–tropospheric exchanges indicated here.

Although the distinction between these two nucleation processes is not of great significance to the current study in relation to the documentation of the appropriate atmospheric structures and the resultant effects on cirrus cloud properties, the lidar depolarization data suggest that both ice nucleation mechanisms may have been active at times. If we equate the atypically high δ values with a dominance of the complicated ice crystal shapes generated from the homogeneous freezing of sulfuric acid droplets, and the unusually low δ values with haze particles derived from relatively large ammonium sulfate CCN particles to yield the variety of crystal shapes commonly observed in cirrus, then the PDL depolarization data could be applied to discriminating the two particle-forming mechanisms at temperatures ≤ -40°C. We note that $\delta \geq 0.55$ were measured only occasionally but predominantly within generating regions near the tops of the lower and upper cirrus cloud layers on the nights of 5 and 6 December, respectively, whereas the strongly scattering $\delta \leq 0.1$ cell heads were found only on 6 December at the tops of the fallstreaks forming the lower layer. This great diversity in lidar depolarization suggests that the stratospheric aerosol content within the cirrus cloud altitude range was variable in time and space.

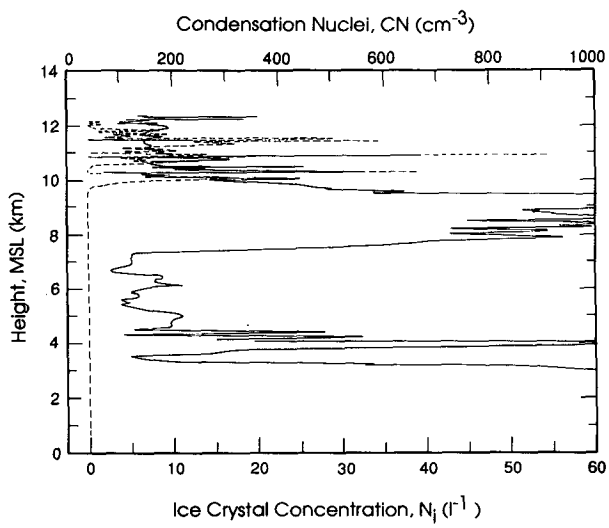

FIG. 17. Vertical profiles of ice crystal (dashed) and CN concentrations, as in Fig. 15, measured from 1915–2021 5 December during the spiral descent of the Citation.

TABLE 3. Soluble mass fraction analysis of aerosol samples collected in situ on 5 December by the NCAR Saberliner assuming the presence of ammonium sulfate (R_{AMS}) or sulfuric acid ($R_{H_2SO_4}$) solutions; N denotes the total CN concentration as measured with a TSI CN counter.

Time (UTC)	Altitude (m)	N (cm^{-3})	R_{AMS}	$R_{H_2SO_4}$
1544	8300	1100	0.10	0.072
1604	9100	1100	0.041	0.030
2028	8850	1800	0.22	0.160

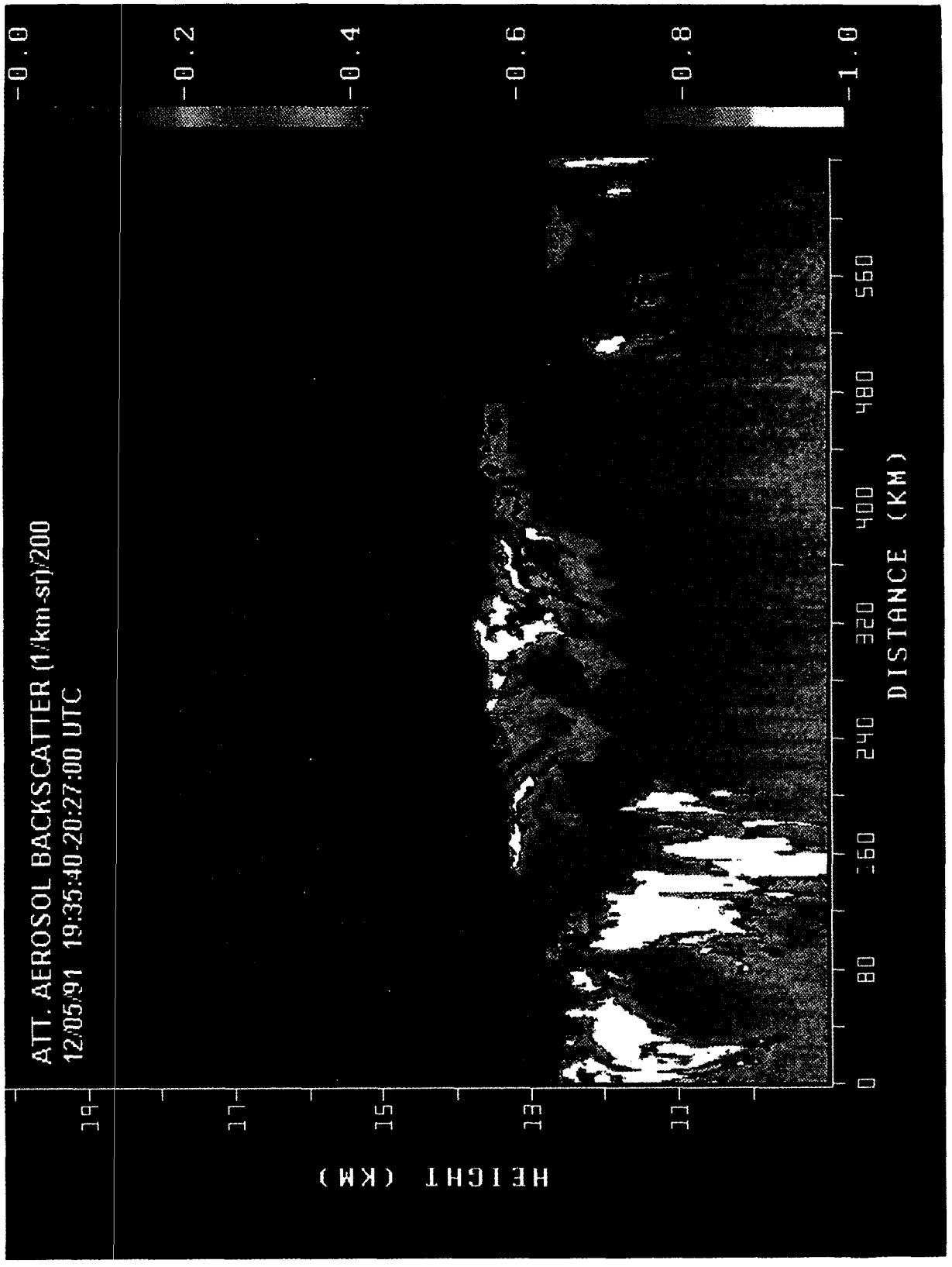

FIG. 18. Height vs distance display of attenuated backscatter coefficients (see key) obtained by the downward-looking ER-2 lidar system from Coffeyville (0-km distance) south to the Houston area. This display has been adjusted to bring out the relatively weak backscattering from lower-stratospheric/upper-tropospheric aerosols, and thus "overexposes" the patchy cirrus clouds also sampled.

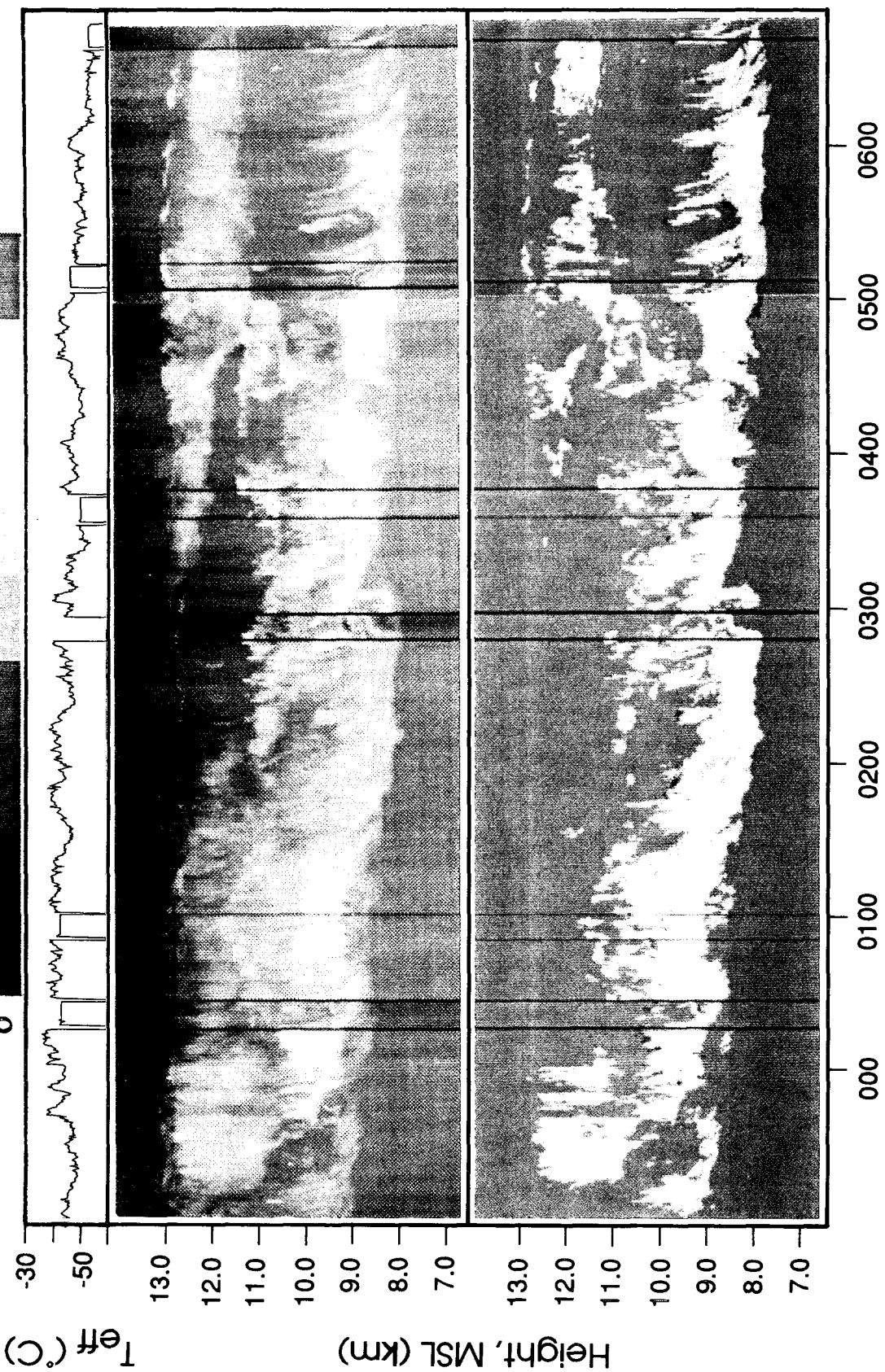

FIG. 19. Polarization lidar HTI displays of relative returned lidar energy (top) and linear depolarization ratios (see at top key) of the cirrus observed on the evening and night of 5–6 December. Infrared radiometer brightness temperatures T_{eff} are shown in the top panel.

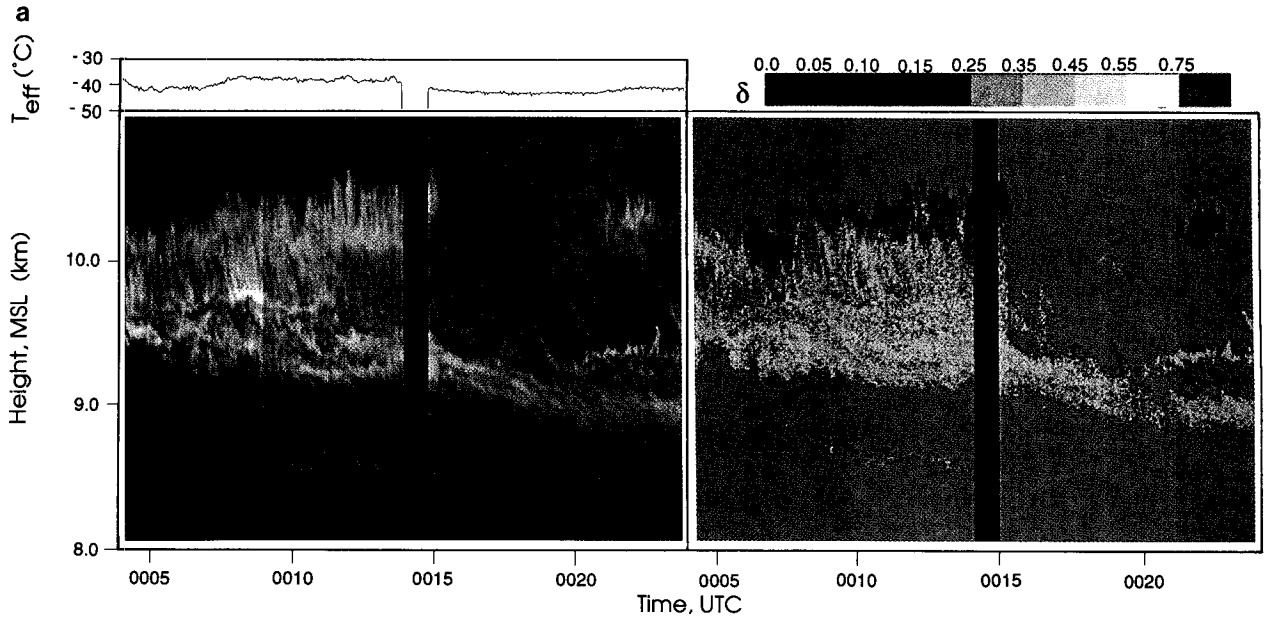

FIG. 20. Details of the high-resolution PDL returned energy and depolarization displays (as in Fig. 11) expanded from Fig. 19 at the indicated times on 6 December, showing complexes of cirrus uncinus cell heads composed mostly of haze droplets with $\delta \leq 0.1$ and the streamers of ice crystals nucleated from them. The uncinus cell head minimum temperatures are −47.3°, −43.0°, and −47.8°C in (a)–(c), respectively.

In terms of the time–height analysis of Fig. 3, it is obvious that opportunities for stratospheric–tropospheric exchanges were provided locally by the passage of jet streaks. A question must be addressed, however, before these changes in atmospheric structure can be related to the formation of cirrus clouds—that is, how are the relatively dry mixed parcels humidified sufficiently to bring about the aerosol growth and ice crystal nucleation processes involved in cirrus generation? We believe that a variety of mixing processes were involved in preparing the stratospheric aerosol for their role as cirrus cloud nuclei. Most notably, the obvious connection between cirrus cloud generation and the boundaries of the elevated frontal zones, as well as the tropopause itself, shows that turbulent and diffusion processes were effective in activating some of the aerosol particles. The local humidification of the mixed stratospheric–tropospheric layers caused by cirrus precipitation and evaporation processes is also clearly indicated and may have aided in the formation of altocumulus at the trailing edges of the cirrus cloud masses. However, since not all of the observed clouds can be linked to identifiable atmospheric structures of recent stratospheric origin, despite the presence at times of greatly elevated CN concentrations, it would appear that advective processes acting on more mixed parcels contained enriched aerosol levels were also prevalent. The in situ aerosol data suggest that considerable spatial inhomogeneity in the aerosol field was present, while at the same time the CO_2-lidar observations demonstrate that the upper troposphere contained a greatly enhanced aerosol content over typical pre-Pinatubo conditions throughout the case study period. This suggests that prolonged stratospheric–tropospheric mixing had taken place in the upstream flow that subsequently swept over the Hub. A long fetch of modified stratospheric air would have had opportunities to become moisturized. For example, according to satellite imagery, large-scale cirrus generation in this case was facilitated by an upwind closed low pressure system over the Baja Peninsula and by orography in the western United States (see Fig. 4).

6. Conclusions

This intensively studied case study from the Project FIRE IFO II campaign has provided an opportunity to examine the effects of a series of jet streaks on the formation of cirrus clouds at midlatitudes. The linkage between jet stream dynamics and cirrus clouds has long been recognized on the basis of satellite imagery (Whitney et al. 1966), and the characteristics of the cirrus have recently been the subject of numerical studies (Durran and Weber 1988).

In this case, however, remote and in situ aerosol and ozone measurements have illustrated that the microphysical processes involved in the formation and maintenance of jet stream cirrus clouds could have been significantly altered by contamination from decaying volcanic debris within six months of the massive Mt. Pinatubo eruptions. Indicated cirrus cloud alterations include abnormally high ice crystal concen-

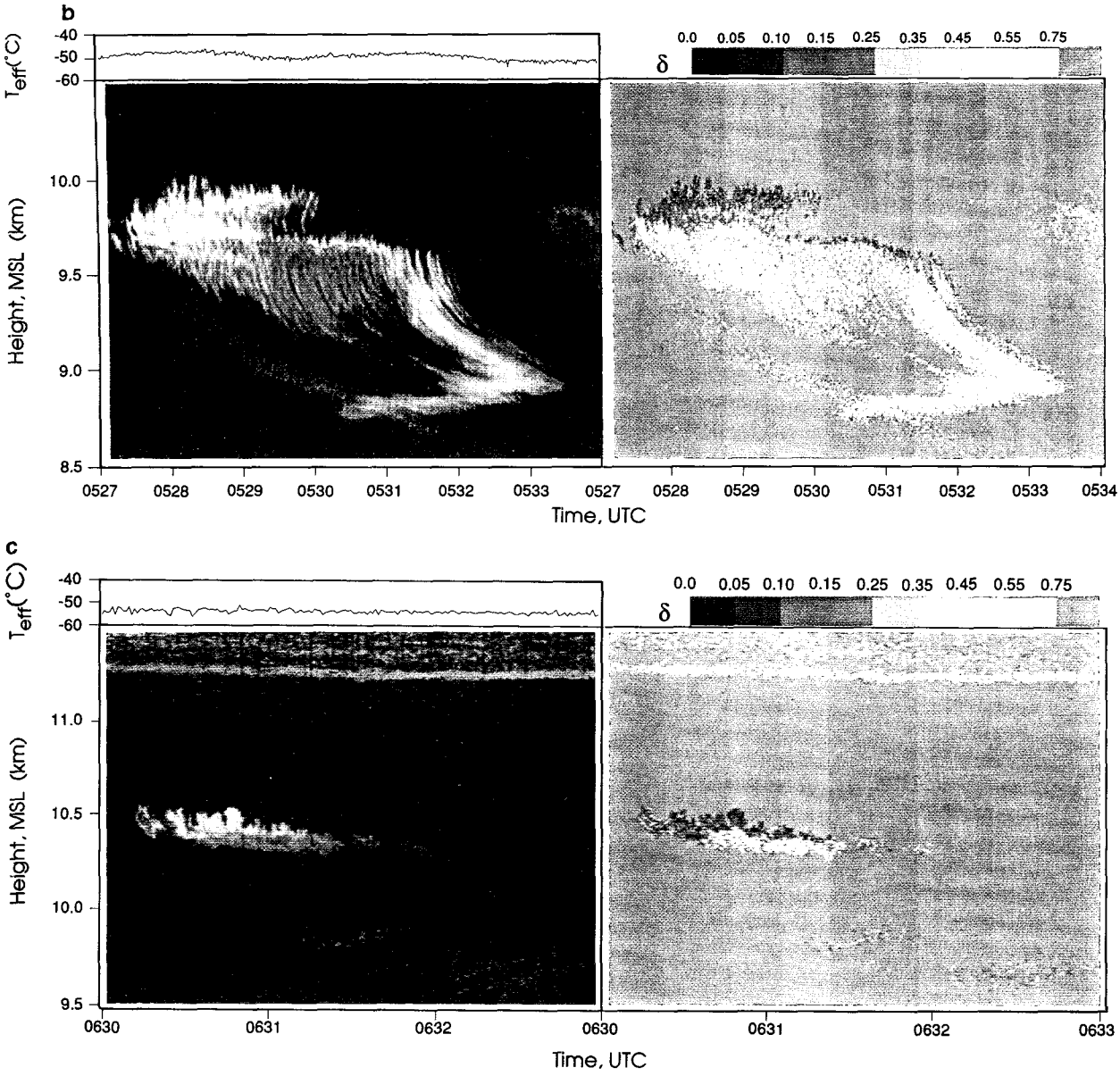

FIG. 20. (*Continued*)

trations (up to ~600 L^{-1}), perhaps unique radial ice crystal shapes, and relatively large haze particles in cirrus uncinus cell heads at temperatures approaching −50°C. These unusual cloud microphysical properties appear to have resulted both from the previous modification of the middle and upper troposphere caused by upwind tropopause foldings and from direct contact with the tropopause and elevated frontal zones. In essence, the local jet streak dynamical processes acted on an atmospheric environment already altered by stratospheric–tropospheric exchanges embedded in the upper-level flow. Although previous lidar research has suggested that the locally observed vertical distribution of volcanic aerosols was influenced by upstream tropopause foldings (Post 1986; Sassen and Horel 1990), it can now be concluded that the continued mixing and dynamical processes experienced by such regions can serve to humidify and condition the aerosol, particularly at the mixed tropospheric–stratospheric interfaces, to make them effective cirrus particle-forming nuclei. The in situ data further suggest that relatively small (on the order of tens of kilometers) aerosol-contaminated parcels were contained within the advecting air flow, presumably the result of the breakup of aging elevated frontal zones that could not be satisfactorily resolved in the available synoptic

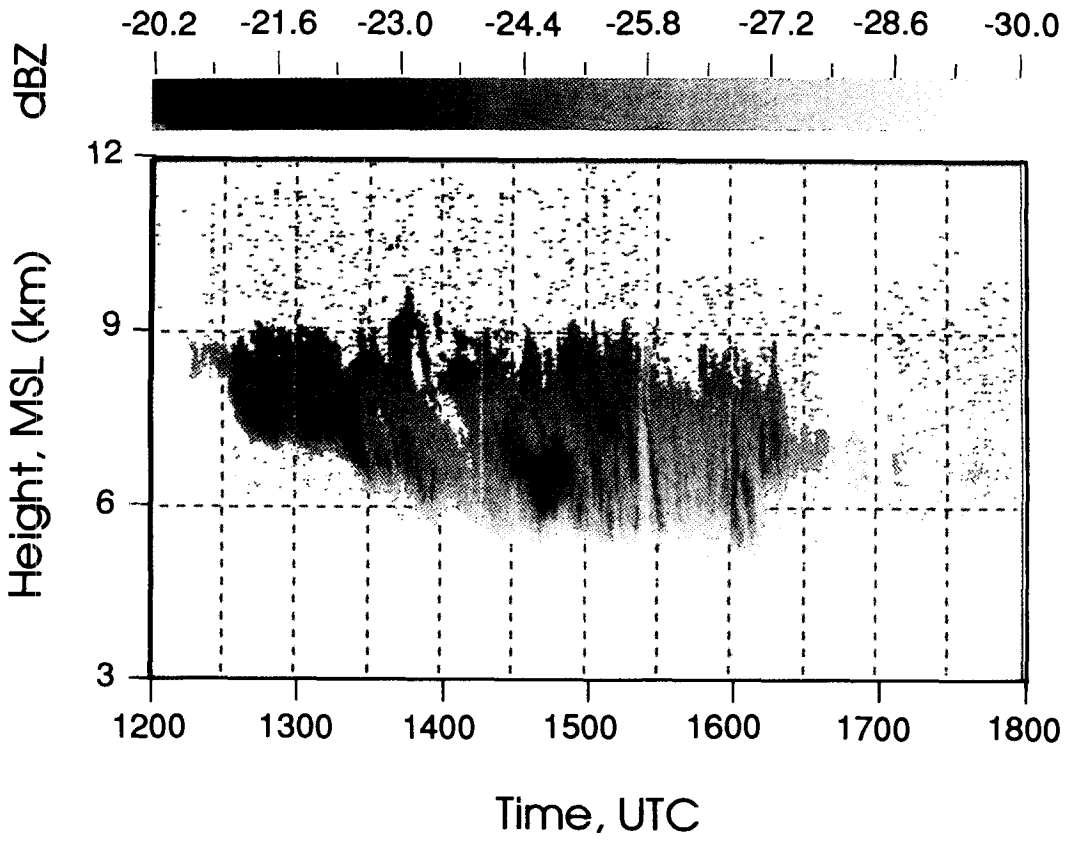

FIG. 21. Height–time radar-reflectivity greyscale display (in dBZ, see key at top) of the cirrus over the Hub during the indicated period on 6 December, as measured by the Pennsylvania State University 94-GHz radar.

data. Interestingly, aircraft ozone concentrations in these parcels tend to be inversely related to CN counts, except at the aerosol-layer boundaries where ozone enhancement was observed, which is suggestive of possible ozone depletion via interactions with the aerosols of stratospheric origin (Hofmann and Solomon 1989; Rodriguez et al. 1994). Basically, these atmospheric conditions were fortuitously observed over the Hub site due to the relative consistency in the upper-level flow over the project area during the case study period.

These findings have implications for "normal" cirrus clouds that form in association with jet streams, and also perhaps for deep tropospheric storm systems that develop along upper-level fronts (Martin et al. 1993). Cirrus cloud–stratospheric aerosol effects need not occur solely in connection with jet streams, however, a fact that has major implications for cirrus cloud formation models ranging from the cloud to GCM scales. Even though the background (i.e., volcanically unperturbed) lower-stratospheric aerosol content is considerably more innocuous, mixing processes provide the upper troposphere with a steady source of aerosols from above (Reiter 1972; Kent et al. 1991). There is already evidence from pre-Pinatubo lidar studies that those midlatitude cirrus with cloud tops extending just above the tropopause have unusual cloud properties, including the generation of corona displays and strong backscattering and depolarization (Sassen 1991). The data presented here from the morning hours of 5 December show what appears to be an analogous occurrence, except that this cirrus layer formed well below the tropopause (and possible corona effects could not be assessed). Cirrus ice particle nucleation from the homogeneous freezing of diluted sulfuric acid droplets of stratospheric origin is indicated to yield a polarization lidar scattering signature when such particles predominate in the cloud (although their presence may go unnoticed when mixed with other particles). The ice crystal photomicrographs in Fig. 13 provide tantalizing indications of the complex nature of the particles that result from the acid droplet freezing process.

It is clear that the apparently distinct nucleation mechanisms involved in the formation of tropopause-topped and some jet stream cirrus clouds from sulfur-based particles have climatic implications, as shown schematically in Fig. 23. In this flow chart the aerosol mixing may be due to gradual turbulence–diffusion or relatively rapid tropopause folding effects, and the moisturizing process to create cirrus particles can in-

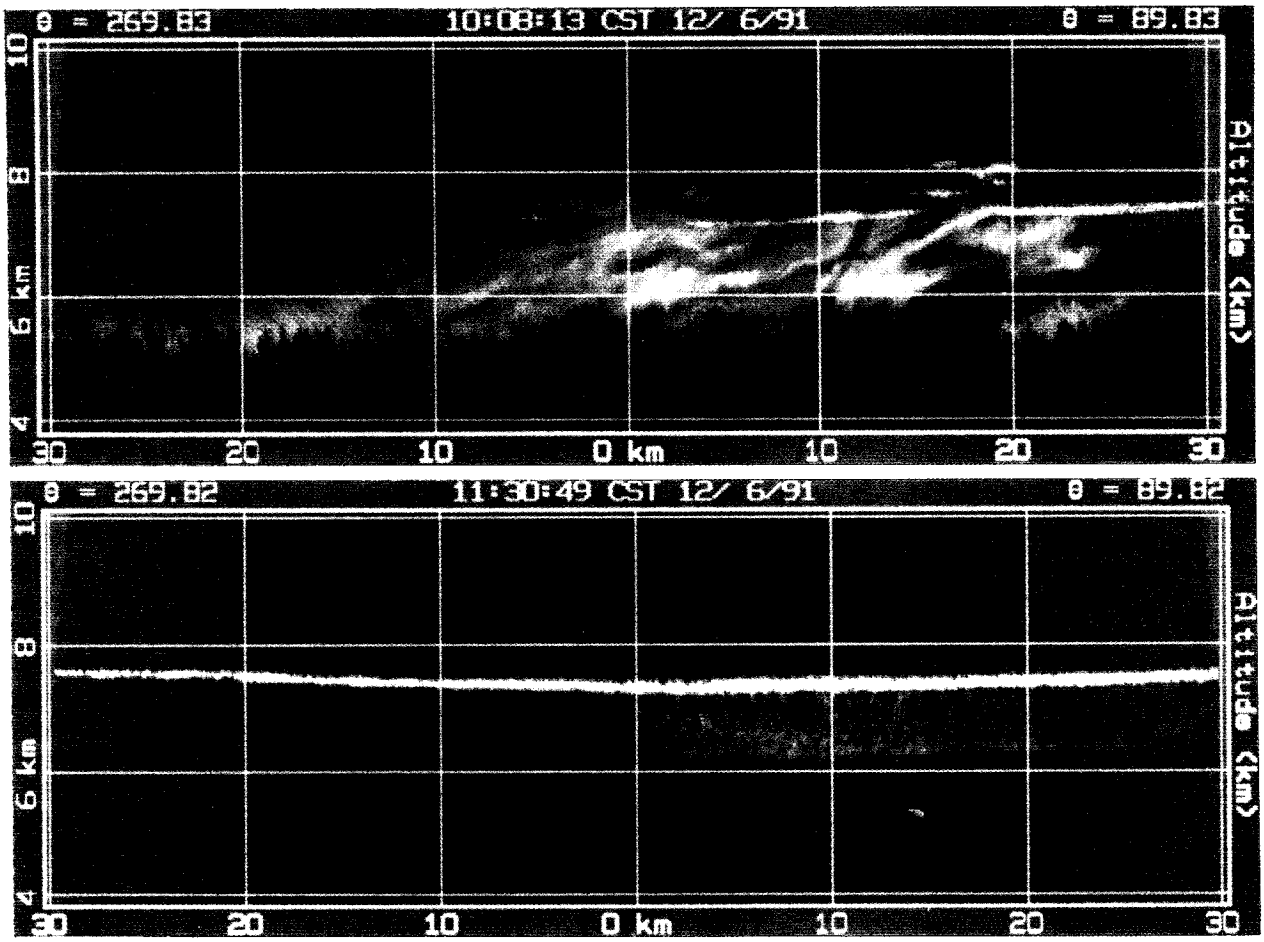

FIG. 22. Volume imager lidar range–height scan displays of the cirrus and altocumulus clouds in the vicinity of the Hub site, collected at (a) 1608 and (b) 1731 6 December. These clouds often produced strong optical attenuation that restricted the depth of lidar probing. This is evident in the left side of the top display, where only the cloud-base region with mammatus-like protrusions was penetrated by the laser.

volve aerosol sedimentation through the hydropause or uplift in connection with jet streaks or other dynamical processes, such as in closed low pressure systems. The key to understanding the climatic effects of volcanically altered cirrus, however, lies in the exact changes that occur in cloud microphysical properties. Although radiative transfer simulations have generally indicated that optically thin cirrus clouds in the upper troposphere contribute to the greenhouse warming effect (e.g., see Liou 1986), the opposite effect, a cooling from increased cirrus cloud solar scattering, could reinforce the albedo increase caused by volcanic aerosols in the stratosphere (Minnis et al. 1993). Assuming, for example, that larger and more abundant CCN are introduced into cirrus cloud altitudes, one might expect from modeling studies that the cirrus would be produced more readily (i.e., at lower relative humidities) and be longer lasting (i.e., drawing from an enlarged CCN population to replenish losses from crystal precipitation). Alternatively, greatly increased CCN concentrations could lead to more gravitationally stable cirrus clouds composed of more numerous small crystals with quite different radiative properties. A further complication is the unusually complex shape of these cirrus crystals, which, according to previous research (Sassen 1991), tends to produce relatively small and highly depolarizing particles near cloud tops until additional diffusional or aggregational growth with other particles causes a change in cloud-scattering properties. Detailed cloud microphysical–radiative simulations tailored to the haze and ice cloud alterations induced by sulfur-based aerosols, using reasonable size distributions, are required to solve this problem, and it is encouraging that first steps in this direction have already been made (Jensen and Toon 1992).

Finally, we note from Fig. 23 that the fate of the stratospheric aerosol in the middle and upper troposphere is likely to be a relatively rapid removal through precipitation processes. In situ measurements have

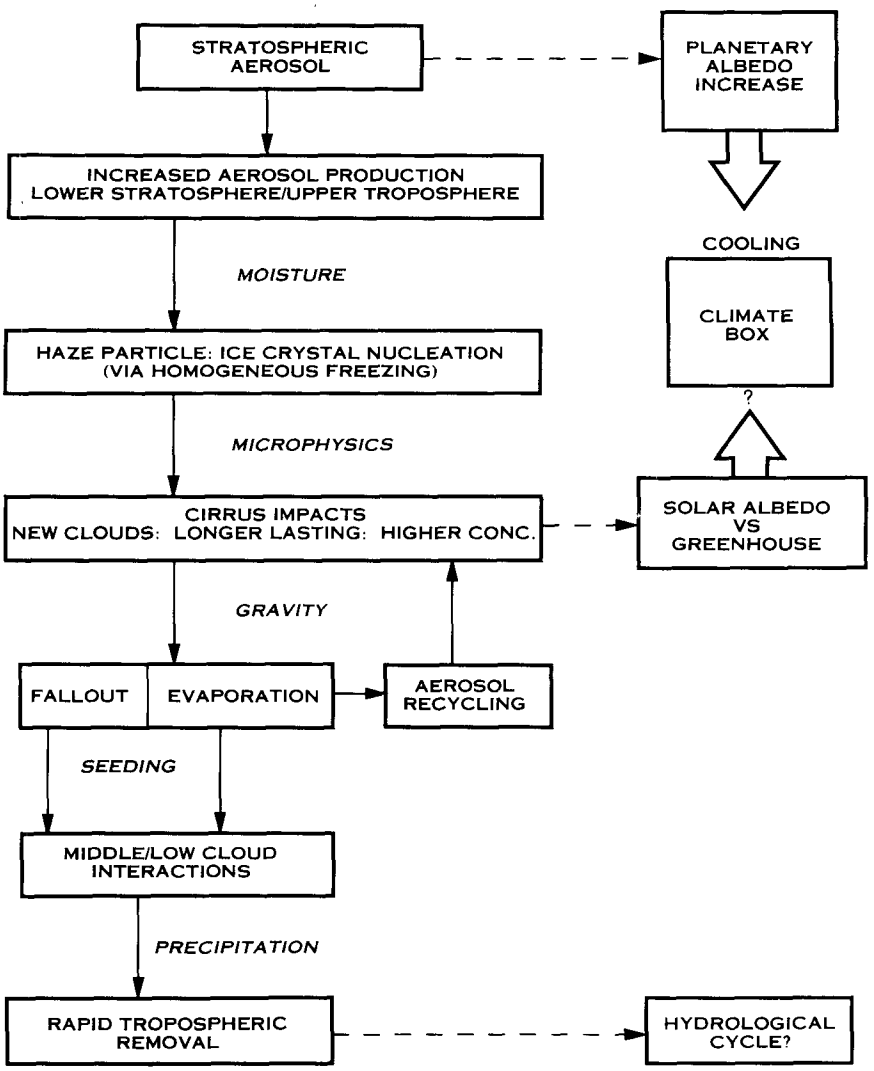

FIG. 23. Schematic representation of the possible climatic effects (right) produced by an influx of volcanic stratospheric aerosols into the troposphere.

shown the significant decline in the sulfuric acid aerosol that occurs in the midtroposphere (Yamato and Ono 1989), a phenomenon that is also suggested by satellite studies (Kent et al. 1991). Although the stratospheric CCN introduced into lower tropospheric clouds may be overwhelmed by the abundant background CCN population derived from the surface, and thus be of little consequence to climate, it is possible that precipitation could be enhanced from cirrus particle seeding effects, thereby affecting the hydrological cycle. This lies clearly outside the scope of this paper, but we can point out that a similar hypothesis was suggested many years ago in connection with the fallout of meteoric dust introduced into the upper atmosphere following major meteor showers (Bowen 1956).

Acknowledgments. Support for the University of Utah FIRE IFO research came from NSF Grant ATM-8914348, which also partially supported the NCAR aircraft operations, and NASA Grant NAG-1-1314: PDL development from DOE Grant DE-FGO2ER1059 of the Atmospheric Radiation Measurement program, which, along with a grant from the NOAA Climate and Global Change Program, also supported the NOAA WPL field operations: University of North Dakota Citation operations from NASA Grant NAG-1-1351: University of Missouri aerosol-sampling efforts from NSF Grant ATM-8820708: and for Pennsylvania State University NASA Grant NAG-1-1095 and a graduate student fellowship from NASA Goddard SFC (for G. G. Mace). Project FIRE NASA funding was provided by the Office of Space Science and Applications under the direction of Dr. J. T. Suttles.

The authors wish to thank the personnel at GSFC (Dave Whiteman, Rich Ferrare, Keith Evans) and San-

dia National Laboratory (John Goldsmith, Scott Bisson, Marshall Lapp) who were responsible for the GSFC Raman lidar data acquisition and analysis, and numerous other FIRE investigators who contributed to the project and made their data available.

REFERENCES

Bigg, E. K., 1975: Stratospheric particles. *J. Atmos. Sci.*, **32,** 910–917.

Bowen, E. G., 1956: The relation between rainfall and meteor showers. *J. Meteor.*, **13,** 162–166.

Cox, S. K., D. S. McDougal, D. A. Randall, and R. A. Schiffer, 1987: FIRE—The First ISCCP Regional Experiment. *Bull. Amer. Meteor. Soc.*, **68,** 114–118.

Danielson, E. F., 1968: Stratospheric–tropospheric exchange based upon radioactivity, ozone, and potential vorticity. *J. Atmos. Sci.*, **25,** 502–518.

Durran, D. R., and D. B. Weber, 1988: An investigation of the poleward edges of cirrus clouds associated with midlatitude jet streams. *Mon. Wea. Rev.*, **114,** 702–714.

Ellingson, R. G., and Coauthors, 1993: The Spectral Radiation Experiment (SPECTRE): Clear-sky observations and their use in ICRCCM and ITRA. *IRS' 92: Current Problems in Atmospheric Radiation,* S. Keevallik and O. Karner, Eds., A. Deepak, 451–453.

Eloranto, E. W., and D. K. Forrest, 1992: Volume imaging lidar observations of the convective structure surrounding the flight path of an instrumented aircraft. *J. Geophys. Res.*, **97,** 18 383–18 394.

Ferrare, R. A., S. H. Melfi, D. N. Whiteman, and K. D. Evans, 1992: Raman lidar measurements of Pinatubo aerosols over southeastern Kansas during November–December, 1991. *Geophys. Res. Lett.*, **19,** 1599–1602.

Friend, J. P., R. Leifer, and M. Trichon, 1973: On the formation of stratospheric aerosols. *J. Atmos. Sci.*, **30,** 465–479.

Georgii, H. W., and W. J. Müller, 1974: On the distribution of ammonia in the middle and lower troposphere. *Tellus,* **26,** 1–2, 180–184.

Global Volcanism Network, *Bulletin of the Smithsonian Institution 1991–1993:* Vols. 17–19 [Available from the American Geophysical Union, Washington, DC.]

Hagen, D. E., A. J. Heymsfield, M. B. Trueblood, and J. Podzimek, 1990: Measurements of upper-tropospheric aerosol characteristics: Implications for cirrus clouds. *Proc. Conf. on Cloud Physics,* San Francisco, CA, Amer. Meteor. Soc. 475–478.

——, M. B. Trueblood, and P. D. Whitefield, 1992: A field sampling of jet exhaust aerosols. *Particulate Sci. & Technol.*, **10,** 53–63.

Heymsfield, A. J., and R. M. Sabin, 1989: Cirrus crystal nucleation by homogeneous freezing of solution droplets. *J. Atmos. Sci.*, **46,** 2252–2264.

Hofmann, D. J., and J. Soloman, 1989: Ozone destruction through heterogeneous chemistry following the eruption of El Chichon. *J. Geophys. Res.*, **94,** 5029–5041.

Jensen, E. G., and O. B. Toon, 1992: The potential effects of volcanic aerosols on cirrus cloud microphysics. *Geophys. Res. Lett.*, **19,** 1759–1762.

Kent, G. S., M. P. McCormick, and S. K. Schaffner, 1991: Global optical climatology of the free tropospheric aerosol from 1.0-μm satellite occultation measurements. *J. Geophys. Res.*, **96,** 5249–5267.

Keyser, D., and M. A. Shapiro, 1986: A review of the structure and dynamics of upper-level frontal zones. *Mon. Wea. Rev.*, **114,** 452–499.

Liou, K. N., 1986: Influence of cirrus clouds on weather and climate processes: A global perspective. *Mon. Wea. Rev.*, **114,** 1167–1199.

Martin, J. E., J. D. Locatelli, and P. V. Hobbs, 1993: Organization and structure of clouds and precipitation on the Mid-Atlantic coast of the United States. Part VI: The synoptic evolution of a deep tropospheric frontal circulation and attendant cyclogensis. *Mon. Wea. Rev.*, **121,** 1299–1316.

Mattocks, C., and R. Bleck, 1986: Jet streak dynamics and geostrophic adjustment processes during the initial stages of lee cyclogensis. *Mon. Wea. Rev.*, **114,** 2033–2056.

Minnis, P., E. F. Harrison, L. L. Stowe, G. G. Gibson, F. M. Denn, D. R. Doelling, and W. L. Smith Jr., 1993: Radiative climate forcing by the Mount Pinatubo eruption. *Science,* **259,** 1411–1415.

Mohnen, V. A., 1990: Stratospheric ion and aerosol chemistry and possible links with cirrus cloud microphysics: A critical assessment. *J. Atmos. Sci.*, **47,** 1933–1948.

Platt, C. M. R., J. C. Scott, and A. C. Dilley, 1987: Remote sounding of high clouds. Part VI: Optical properties of midlatitude and tropical cirrus. *J. Atmos. Sci.*, **44,** 729–747.

Post, M. J., 1986: Atmospheric purging of El Chichón debris. *J. Geophys. Res.*, **91,** 5222–5228.

——, C. J. Grund, A. O. Langford, and M. H. Proffitt, 1992: Observations of Pinatubo ejecta over Boulder, Colorado, by lidars of three different wavelengths. *Geophys. Res. Lett.*, **19,** 195–198.

Reiter, E. R., 1972: *Atmospheric Transport Processes, Part 3: Hydrodynamic Tracers.* U.S. Atomic Energy Commission Critical Review Series, USAEC Report TID-24868, 212 pp. [NTIS TID-25731.]

Rodríguez, J. M., M. K. W. Ko, N. D. Sze, and C. W. Heisey, 1994: Ozone response to enhanced heterogeneous processing after the eruption of Mt. Pinatubo. *Geophy. Res. Lett.*, **21,** 209–212.

Rubel, G. O., and J. W. Gentry, 1985: Onset of particle crystallization resulting from acid droplet ammonia gas reactions. *J. Aerosol Sci.*, **18,** 23–27.

Sassen, K., 1991: Corona-producing cirrus cloud properties derived from polarization lidar and photographic analyses. *Appl. Opt.*, **30,** 3421–3428.

——, 1992: Evidence for liquid-phase cirrus cloud formation from volcanic aerosols: Climatic implications. *Science,* **257,** 516–519.

——, and G. C. Dodd, 1989: Haze particle nucleation simulations in cirrus clouds and applications for numerical and lidar studies. *J. Atmos. Sci.*, **46,** 3005–3014.

——, and J. D. Horel, 1990: Polarization lidar and synoptic analyses of an unusual volcanic aerosol cloud. *J. Atmos. Sci.*, **47,** 2881–2889.

——, H. Zhao, and B.-K. Yu, 1989: Backscatter laser depolarization studies of simulated stratospheric aerosols: Crystallized sulfuric acid droplets. *Appl. Opt.*, **28,** 3024–3029.

——, C. J. Grund, J. Spinhirne, M. Hardesty, and J. M. Alvarez, 1990: The 27–28 October 1986 FIRE IFO cirrus case study: A five lidar overview of cloud structure and evolution. *Mon. Wea. Rev.*, **118,** 2288–2311.

Schiffer, R. A., and W. B. Rossow, 1983: The International Satellite Cloud Climatology Project (ISCCP): The first project of the World Climate Research Programme. *Bull. Amer. Meteor. Soc.*, **64,** 779–784.

Shapiro, M. A., 1976: The role of turbulent heat flux in the generation of potential vorticity in the vicinity of upper-level jet stream systems. *Mon. Wea. Rev.*, **104,** 892–906.

——, R. C. Schnell, F. P. Parungo, S. J. Oltmans, and B. A. Bodhaine, 1984: El Chichón volcanic debris in an Arctic tropopause fold. *Geophys. Res. Lett.*, **11,** 421–424.

Starr, D. O'C., and S. K. Cox, 1988: Cirrus clouds. Part II: Numerical experiments on the formation and maintenance of cirrus. *J. Atmos. Sci.*, **42,** 2682–2694.

Whiteman, D. N., S. H. Melfi, and R. A. Ferrare, 1992: Raman lidar system for the measurement of water vapor and aerosols in the earth's atmosphere. *Appl. Opt.*, **31,** 3068–3082.

Whitney, L. F., Jr., A. Timchalk, and T. I. Gray Jr. 1966: On locating jet streams from TIROS photographs. *Mon. Wea. Rev.*, **94,** 127–138.

Yamato, M., and A. Ono, 1989: Chemical and physical properties of stratospheric aerosol particles in the vicinity of tropopause folding. *J. Meteor. Soc. Japan,* **67,** 147–165.